

Article

Blast Loading of Small-Scale Circular RC Columns Using an Explosive-Driven Shock Tube

Mohamed Ben Rhouma ^{1,2,*} , Azer Maazoun ³ , Aldjabar Aminou ^{1,2} , Bachir Belkassem ¹,
Ignaas Vandenbruwane ⁴, Tine Tysmans ²  and David Lecompte ¹

¹ Structural and Blast Engineering Department, Royal Military Academy, Avenue de la Renaissance 30, 1000 Brussels, Belgium; aldjabar.aminou.malam.kailou@vub.be (A.A.); bachir.belkassem@mil.be (B.B.); david.lecompte@mil.be (D.L.)

² Mechanics of Materials and Constructions Department, Vrije Universiteit Brussels, Pleinlaan 2, 1050 Brussels, Belgium; tine.tysmans@vub.be

³ Civil Engineering Department, Military Academy of Fondouk Jedid, Nabeul 8021, Tunisia; azer.maazoun@ugent.be

⁴ Magnel Laboratory for Concrete Research, Ghent University, Technologiepark-Zwijnaarde 904, 9052 Gent, Belgium; ignaas.vandenbruwane@ugent.be

* Correspondence: mohamed.benrhouma@mil.be

Abstract: Reinforced concrete (RC) columns, being axial-bearing components in buildings, are susceptible to damage and failure when subjected to blast loading. The failure of these columns can trigger a progressive collapse in targeted buildings. The primary objective of this study is to investigate the failure characteristics of laboratory-scale RC columns subjected to localized blast loading. The columns, with a length of 1500 mm and an outer diameter of 100 mm, are reinforced with 6 mm diameter longitudinal bars and 2 mm diameter steel ties. The blast loading is generated using an explosive-driven shock tube (EDST) positioned in front of the mid-span of the RC columns with a 30 g and 50 g charge. To capture the global response of the RC columns, high-speed stereoscopic DIC is used in addition to LVDTs. Furthermore, an FE model is developed using LS-DYNA R10.0 and validated against the experimental data. The results show that the proposed FE approach is able to reproduce the applied blast loading and the failure characteristics of the columns. The relative difference in column mid-span out-of-plane displacement between the FE model and the average measured data lies below 5%. Finally, the gray correlation method is conducted to assess the influence of various parameters on the blast resistance of the RC columns.

Keywords: laboratory-scale RC column; numerical analysis; blast response; high-speed stereoscopic DIC; EDST; gray correlation method



Citation: Rhouma, M.B.; Maazoun, A.; Aminou, A.; Belkassem, B.; Vandenbruwane, I.; Tysmans, T.; Lecompte, D. Blast Loading of Small-Scale Circular RC Columns Using an Explosive-Driven Shock Tube. *Buildings* **2024**, *14*, 921. <https://doi.org/10.3390/buildings14040921>

Academic Editor: Bo-Tao Huang

Received: 2 March 2024

Revised: 21 March 2024

Accepted: 24 March 2024

Published: 27 March 2024



Copyright: © 2024 by the authors. Licensee MDPI, Basel, Switzerland. This article is an open access article distributed under the terms and conditions of the Creative Commons Attribution (CC BY) license (<https://creativecommons.org/licenses/by/4.0/>).

1. Introduction

In the year 2022, the Explosive Violence Monitoring Project documented a total of 31,273 fatalities and injuries attributed to the use of explosive weapons across the globe [1]. Over the past two decades, the frequency of incidents involving explosives has increased by a factor of five. These explosive events nearly always have a significant impact on civilian populations and military personnel [2].

In 1995, a terrorist attack targeted the Alfred P. Murrah building, resulting in 268 fatalities and severe damage to adjacent structures. The blast loading originated from the detonation of a vehicle-borne improvised explosive device (VBIED) containing approximately 1818 kg of equivalent TNT positioned near the target. This bombing caused several non-redundant exterior RC columns to fail. The remaining structural elements were unable to effectively redistribute the load from the upper part of the structure, and consequently, this led to the collapse of a significant part of the building [3].

Examining structures, structural components and materials under blast loading remains essential. The analysis of blast-loaded members can be conducted through three

primary approaches: analytical, numerical and experimental. The analytical approach involves simplified methodologies, including the single-degree of freedom (SDOF), multi-degree of freedom (MDOF) and pressure–impulse (PI) diagrams, commonly found in [4–6]. The second approach involves performing finite element simulations, incorporating blast load parameters obtained from empirical charts found in guidelines [4,5], Kingery and Bulmash [7] or explicit modeling of the detonation process by using constitutive models and equations of state for both air and the specific explosive under consideration [8]. The third approach entails executing blast tests on full-scale models. The first approach has certain limitations, including challenges in predicting specific failure modes in structural members, particularly in scenarios involving close-range explosions [9,10]. The second approach demands important computational power and relies on calibrated or validated material models derived from experimental testing. On the other hand, full-scale tests necessitate expensive and sophisticated instrumentation, typically susceptible to weather conditions [11]. In contrast to full-scale tests, laboratory-scale experiments are more cost-effective and enable experiments to be conducted under controlled testing conditions [12–14]. Laboratory-scale experiments can be a valuable tool for conducting blast analyses of structures and materials.

The common method for subjecting structures to blast loading involves the unconfined detonation of high explosives (HEs). However, in close-range explosions, factors such as slight variations in the shape, position and quantity of the explosive charge can influence the blast wave parameters [15,16]. Furthermore, numerous researchers have documented challenges related to test repeatability, the non-uniform distribution of blast loading in open-air detonations and reduced visibility arising from fireball and dust clouds [17–19]. Hence, shock tubes can serve as a substitute for open-air detonations [20,21]. A gas-driven shock tube is composed of a cylindrical tube with two sections: a high-pressure or driver section and an atmospheric pressure or driven section. A narrow diaphragm serves as the separator between these two sections. The rupture of the diaphragm results in the instantaneous expansion of the driver gas, generating a shock wave that propagates within the driven section [22,23]. It has been noted that the rupture of the diaphragm can lack reproducibility, giving rise to variations in the blast loading parameters [24,25].

An alternative method for generating blast loading is the explosive-driven shock tube (EDST). Positioned between the explosive charge and the component to be loaded, the EDST has demonstrated its utility as a laboratory-scale blast-loading tool, capable of producing significant reflected pressure and impulse values. As part of a comparative study, Louar et al. [11] conducted laboratory-scale experiments to investigate blast wave generation through two methods: unconfined detonation and the explosive-driven shock tube (EDST). The presented findings indicate that the explosive-driven shock tube (EDST) approach achieves higher reflected pressure and impulses with smaller charges. For instance, detonating a 20 g spherical charge of C4 in front of the EDST resulted in significantly higher incident pressure (10,800 kPa) and impulse (1650 Pa.s) at the tube's exit compared to the values recorded for the same explosive mass at the same distance using an unconfined detonation (1100 kPa and 380 Pa.s).

To investigate the dynamic response of laboratory-scale RC columns under blast loading generated by a shock tube, three challenges need to be addressed. The first challenge is the determination of the blast loading. The second one resides in the conception and design of a laboratory-scale experimental setup. The third involves developing a high-fidelity finite element model capable of capturing the interaction between the localized shock wave and the RC column and able to accurately simulate the behavior of the laboratory-scale RC column under blast loading.

Numerous studies have been conducted to examine the dynamic response of RC columns under both distant and close-in explosion scenarios. Initially, an explosion is typically categorized as a close-in blast event when the scaled distance $Z < 1.054 \text{ kg/m}^{1/3}$ [26] or $z < 1.2 \text{ kg/m}^{1/3}$ [27]. The scaled distance Z is defined as $R/W^{1/3}$, where R represents the stand-off distance or the separation between the center of the explosive charge and

the structure, and W denotes the explosive charge mass. In the context of a close-in event, certain researchers have conducted experiments aimed at evaluating the impact of blast and column-related parameters on the dynamic response of RC columns. Woodson et al. [18] conducted a series of five experiments involving quarter-scale RC columns integrated into scaled two-story RC frames subjected to close-in explosions. The test specimens featured a cross-section of $89\text{ mm} \times 89\text{ mm}$ and a height of 935 mm . A hemispherical C-4 charge weighing 7.1 kg was positioned 229 mm above the ground, with a stand-off distance of 1520 mm and 1070 mm facing the nearest exterior RC column. The findings indicate that an increase in the scaled distance resulted in reduced damage to the test columns. Braimah et al. [19] further explored the experimental investigation of the influence of scaled distance and detailing of RC columns. Sixteen full-scale RC columns, consisting of both conventional and seismically detailed columns. Both types of columns had a cross-section of $300\text{ mm} \times 300\text{ mm}$ and a height of 3200 mm . These specimens were exposed to close-in explosions generated by 100 kg and 150 kg of ANFO positioned at distances of 1100 mm , 2700 mm and 4300 mm . Comparing the results, seismic detailing leads to a higher blast-bearing capacity of the RC columns subjected to close-in explosions compared to their conventional counterparts. The continuous progress in finite element modeling enables the increasingly realistic numerical modeling of RC columns under specific blast scenarios. The experimental findings referenced in [18] have served as a validation benchmark for the numerical work of numerous researchers [10,28,29]. The data were used to validate their numerical models and conduct parametric analyses. The evidence indicates that parameters such as concrete strength [30], column detailing [31–35], column dimensions [36], column shape [31,37,38] and axial load ratio [31,39,40] significantly influence the extent of damage in RC columns. Additionally, the impact of explosive mass, shape and scaled distance on the damage and deformation behavior of the blast-loaded columns is also evaluated [9,31]. A significant amount of attention has been directed toward RC columns with section shapes other than circular ones. This work aims to fill this gap in the existing literature.

A novelty of this work, in addition to prior research, lies in its development of a laboratory-scale methodology tailored for assessing the blast behavior of circular RC columns. This methodology integrates the use of the EDST as a laboratory blast tool and DIC for comprehensive analysis of deformation patterns and failure mechanisms. Furthermore, the gray relation method is adopted to evaluate the influence of various parameters on the dynamic response of circular RC columns under EDST-generated blast loading.

Using a validated numerical model, the present study expands the range of testing conditions and explores the impact of a number of parameters on the blast resistance of RC columns, i.e., the diameter of the longitudinal bars ϕ_L , the number of the longitudinal bars n_L , the diameter of the ties ϕ_t , the spacing of the ties s_t , the strength of the concrete s_c , the mass of the explosive charge at the entrance of the EDST m_e and the load eccentricity, h_r . The gray correlation method is adopted to quantify the strength of their correlation. Numerous researchers have used this methodology across diverse fields [35,41,42].

The objectives of this paper are the following:

1. The measurement and simulation of the reflected pressure and impulse on the columns due to the EDST-generated blast loading.
2. An investigation of the dynamic behavior of blast-loaded laboratory-scale RC columns.
3. An investigation of the sensitivity of the dynamic response of the RC columns using the gray correlation method.

This paper is organized into five main sections. First, a detailed explanation of the experimental setup is provided, including details about the laboratory-scale blast-loading tool used. Then, an overview of the adopted finite element approach using the LS-Dyna software is presented. Third, a comparison between the numerical results and the experimental data gathered in the previous section is presented. Subsequently, a sensitivity analysis is conducted to study the influence of the RC column and blast loading-related

parameters on the dynamic response of the RC members. Finally, the paper concludes with a summary of the findings.

2. Layout of the Test Setup

2.1. General Description

All the columns are tested under an EDST-generated blast loading using a spherical C4 charge as shown in Figure 1. The explosive charges have masses of 30 and 50 g. They are positioned at the entrance of the EDST. The charge is initiated using an electric detonator positioned at the back of the explosive. A close-up view of the explosive charge and the detonator is seen in Figure 1a and Figure 7a. The steel frame allows for the height of the EDST to be controlled. The thickness of the aluminum column is selected to guarantee enough rigidity and to avoid deformation during the reflected pressure and impulse measurements. The EDST used in this study consists of a cylindrical steel tube with specific dimensions: an inner diameter of 100 mm, a wall thickness of 10 mm and a length of 800 mm. To withstand the high pressure generated upon detonating the explosive mass at the entry point, the initial 300 mm of the tube is reinforced with an additional steel tube as shown in Figure 1a and Figure 7b. This secondary tube has a thickness of 10 mm and an inner diameter of 135 mm. The gap between these two steel tubes is filled with steel fiber-reinforced concrete.

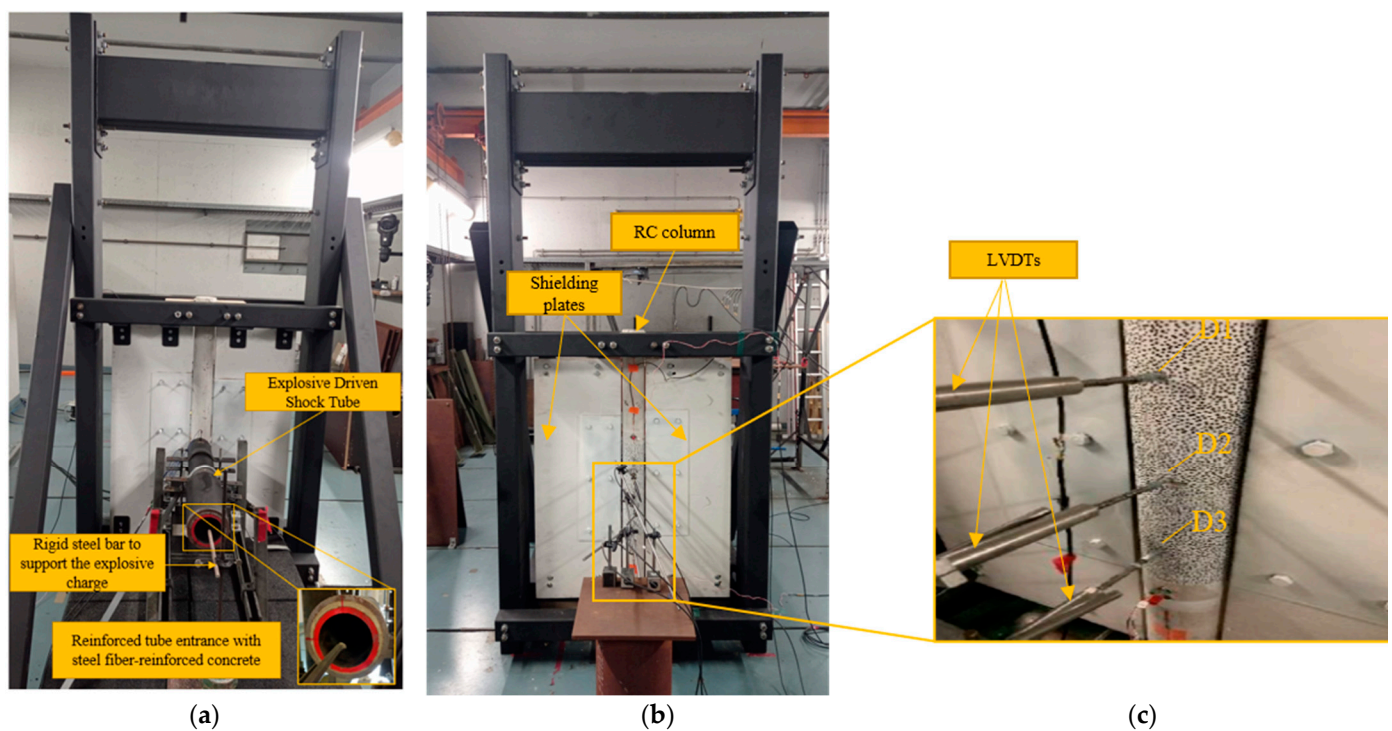


Figure 1. Experimental setup showing (a) the EDST and (b,c) the LVDTs used to capture the out-of-plane displacement of the columns.

A steel structure is used to maintain the test column in a vertical position. Shielding plates 1480 mm long, 1200 mm wide and 20 mm thick are placed on both sides of the specimens. Their objective is to prevent the light flash and detonation gases from interfering with the measurement equipment located behind the specimen. LVDTs and high-speed stereoscopic DIC are used for the measurement of the out-of-plane displacements as shown in Figures 1 and 2. Steel tubes with a thickness of 4 mm, exterior diameter of 40 mm and length of 300 mm are used at both ends of the column to ensure a pinned–pinned configuration.

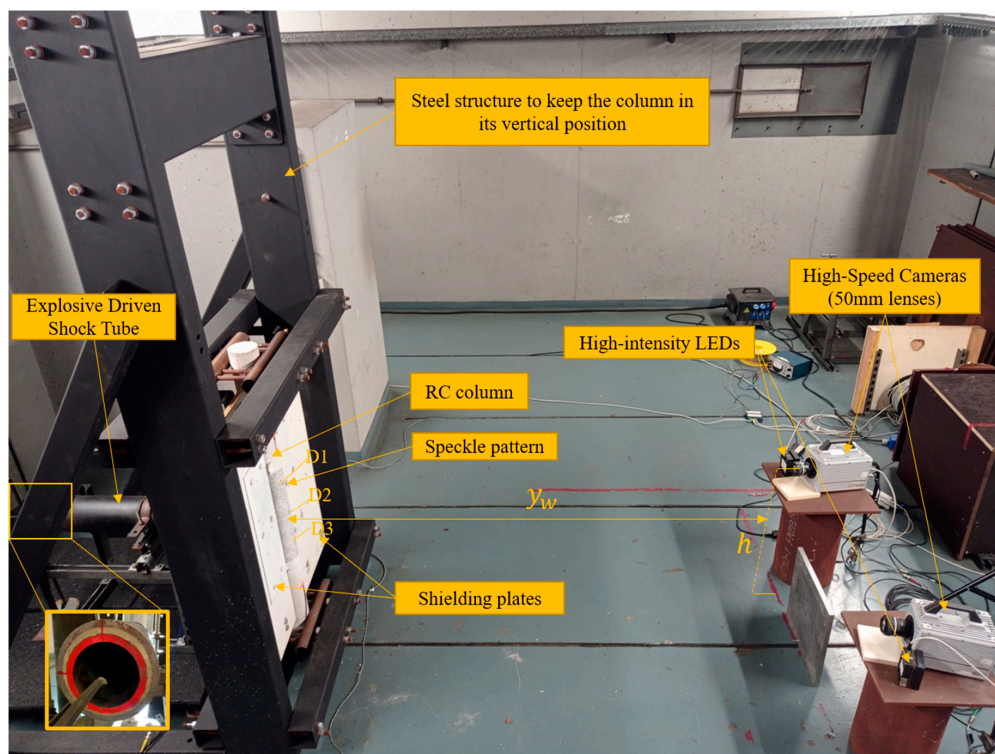


Figure 2. Experimental setup for the out-of-plane displacement measurement of the columns using the digital image correlation technique.

Six RC columns are tested under two different blast loadings. Tests 1, 2 and 3 involve RC columns exposed to 30 g of C4 at the entrance of the EDST, whereas tests 4, 5 and 6 involve RC columns subjected to 50 g of C4.

2.2. Description of the Test Specimens

A detailed configuration of the RC columns is shown in Figure 3. The specimens have a circular section with a diameter of 100 mm and a height of 1500 mm. All the columns are reinforced with 6 mm diameter longitudinal reinforcement and with 2 mm diameter ties. These dimensions are in accordance with the literature [28,30,43–48]. The tie spacing is indicated in Figure 3. The concrete cover has a thickness of 10 mm. The column casting process is shown in Figure 4. The approach consists of the preparation of the reinforcement cage, the preparation of the formwork, the mixing of the concrete components and the pouring of the columns and the concrete blocks for compressive strength determination. Ready-mix concrete, with the cement grade P.O. 32.5 and aggregate size ranging from 2 mm to 8 mm, was used to cast the specimens.

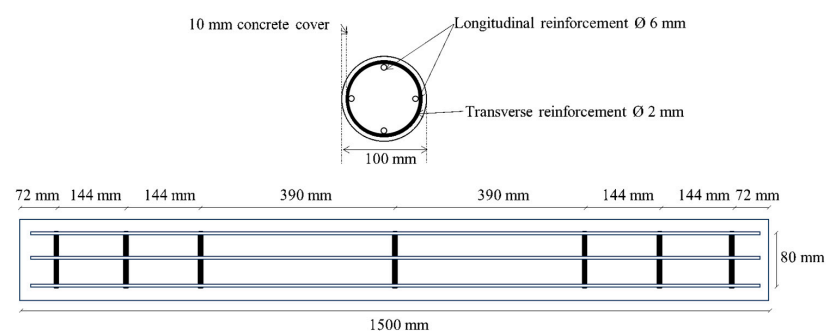


Figure 3. Column design details.



Figure 4. Column casting process: (a) preparation of the reinforcement cage, (b) preparation of the formwork, (c) mixture of the concrete components, (d) column pouring and (e) concrete block pouring.

2.3. Mechanical Properties of Concrete and Reinforcement Steel

To calibrate the numerical model for further simulations, quasi-static tests on concrete and the reinforcement bars are carried out. The properties of the reinforcement steel are obtained based on tensile tests according to NBN EN ISO 6892-1 [49].

Three tests are conducted to ensure the reproducibility of the results. The longitudinal reinforcement bars have a yield strength of 650 ± 22.98 MPa, while the transverse reinforcement has a yield strength of 443 ± 16.68 MPa. The stress–strain curves for the steel reinforcement are shown in Figure 5. Table 1 displays the stresses and strains at the point of yielding and the ultimate strength and rupture for each bar type. The average uniaxial compressive strength of the concrete after curing for 28 days is 32 ± 0.45 MPa measured using three concrete cubes of $150 \text{ mm} \times 150 \text{ mm} \times 150 \text{ mm}$ according to NBN EN 12390-3 [50]. The stress–strain curves for the concrete are shown in Figure 6.

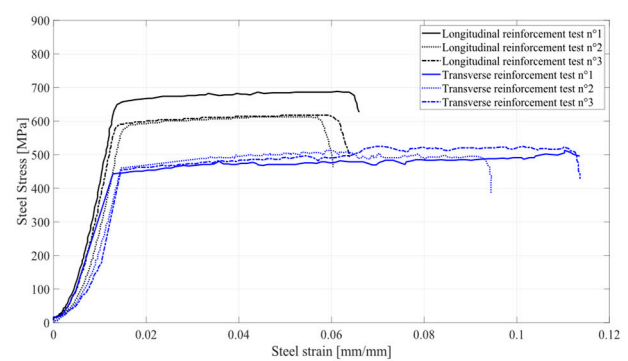


Figure 5. Steel material test.

Table 1. Mechanical properties of the internal reinforcement.

Bar	Diameter (mm)	Young's Modulus (GPa)	Yield		Ultimate	
			Strain (-)	Stress (MPa)	Strain (-)	Stress (MPa)
Longitudinal	6	209 ± 1.53	0.0031 ± 0.0057	650 ± 22.98	0.064 ± 0.0024	686 ± 15.28
Transverse	2	199 ± 3.11	0.0021 ± 0.0032	443 ± 16.68	0.113 ± 0.0017	513 ± 7.07

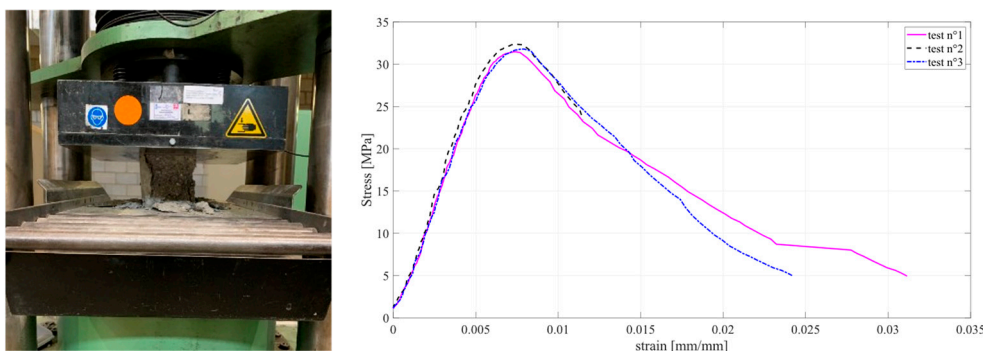


Figure 6. Concrete material test.

2.4. Linear Variable Displacement Transducers (LVDTs)

The displacement at three specific positions, which are the mid-span of the RC column and points located 150 mm at both sides of the mid-span, is measured using Solartron linear variable displacement transducers (S-LVDTs) as shown in Figure 1. The displacement sensors have a maximum stroke of 150 mm. They are fixed to a steel base at one end and attached to the specimen at the other end. The sensors are labeled from top to bottom as D1, D2 and D3, respectively, as shown in Figure 1b,c. The sensor extremity in contact with the specimen is fixed to the column to enable the measurement of both inbound and rebound displacements.

2.5. Displacement Measurements Using High-Speed Stereoscopic DIC

High-speed stereoscopic digital image correlation (DIC) is an optical measurement technique based on a series of images taken by two high-speed cameras. Two synchronized Photron Fastcam SA5 high-speed cameras are positioned in a stereoscopic configuration facing the opposite side of the loading (Figure 2). The distance between the two high-speed cameras and the specimen is 1500 mm. A high-contrast speckle pattern is applied to the area of interest of the RC column facing the two cameras. Positioned at a height (h) of 600 mm, the cameras focus on the central part of the test specimens. To capture the dynamic response of the columns, a frame rate of 20,000 fps is chosen, accompanied by a shutter time of 30 μ s. The aperture of both lenses (Nikkor 50 mm) [51] is adjusted to increase the depth of view. This adjustment limits the amount of incoming light. The specimens are illuminated using two high-intensity LEDs. The observed area of interest is about 157 mm \times 300 mm and is imaged with 512 \times 512 pixels.

3. Experimental Campaign

3.1. Blast Load Characterization

In the first phase, a 5 mm thick aluminum column with a 100 mm outer diameter and a length of 1200 mm is used. The EDST is positioned at mid-height of the column at a distance of 4 mm to generate the blast loading (Figure 7a). The thick-walled aluminum column is provided with a pressure sensor as shown in Figure 7b. A high-frequency pressure sensor (PCB QUARTZ ICP 113 B22 [52]) model is used with a sampling frequency of 1 MHz [11].

The objective of the first test campaign is to determine the reflected pressure and impulse applied to the test specimens. To avoid damage to the pressure transducer, a maximum quantity of 20 g of explosive charge is used in the tests.

To ensure reproducibility, three tests are conducted for each configuration. Due to the high-frequency nature of the measurement noise, a second-order low-pass Butterworth filter is used in MATLAB R2021a [11,53]. Figure 8 and Figure 10a show the reflected pressures and impulses as a function of time at the position of the pressure sensor inserted in the column for a 10 g C4 charge. The reflected pressure–time histories and impulse–time histories for a 20 g C4 are shown in Figures 9 and 10b. These blast wave parameters locally reproduce those of an actual explosion involving 11 kg of TNT at a stand-off distance of

1.4 m and 36 kg of TNT at a stand-off distance of 1.6 m from the target for the case of 10 g and 20 g at the entrance of the EDST, respectively [4]. This observation underscores the blast loading potential achievable by the EDST, even with 10 g and 20 g of C4. The reflected overpressure–time histories shown in Figures 8 and 9 are truncated at 1.6 ms as no discernible variation is observed beyond this point. It can be noted that the signals obtained from the pressure sensor attached to the aluminum column contain some noise. Considering (a) the noise in the measurement and (b) the damage of the pressure sensor due to the high reflected pressure and impulse under 30 g and 50 g of C4, the decision is made to use the results corresponding to the 10 g and 20 g charges to validate the numerical model for the blast loading part.

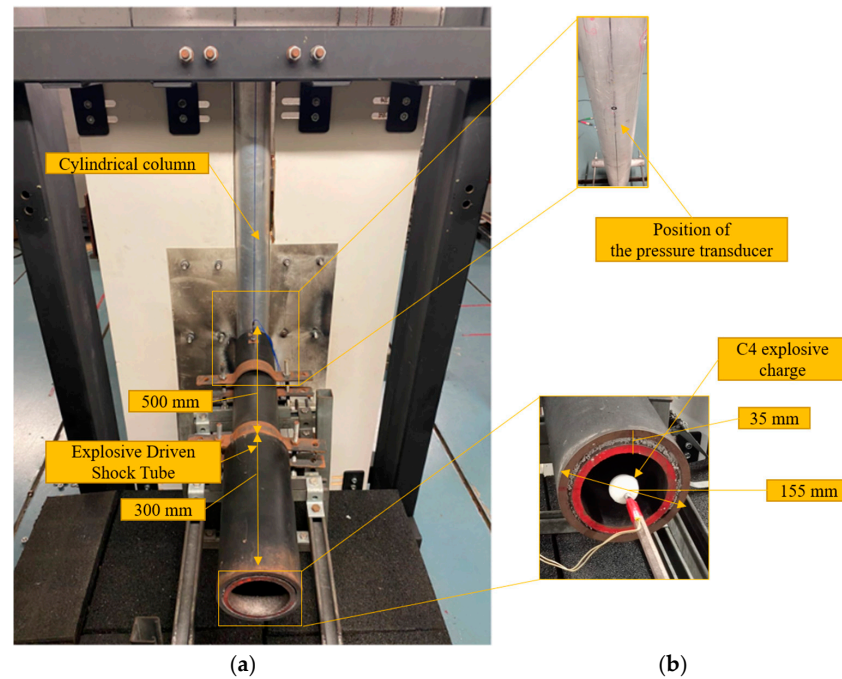


Figure 7. Experimental setup indicating (a) the EDST with the explosive charge, the cylindrical column target and (b) the position of the different pressure gauges.

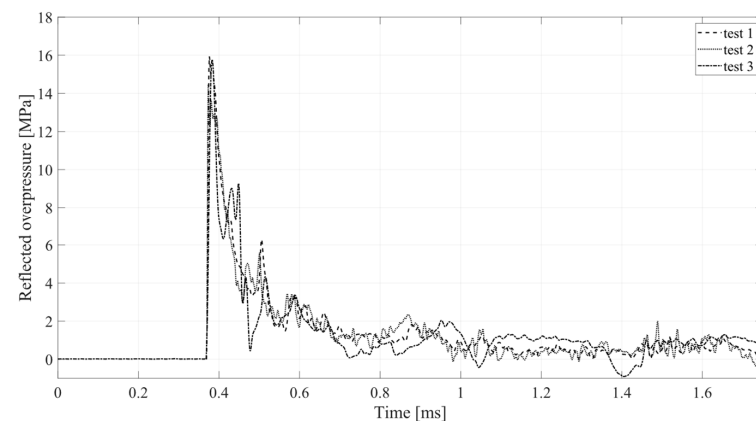


Figure 8. Reflected overpressure–time signals from the column sensor for a charge of 10 g of C4 for three different tests.

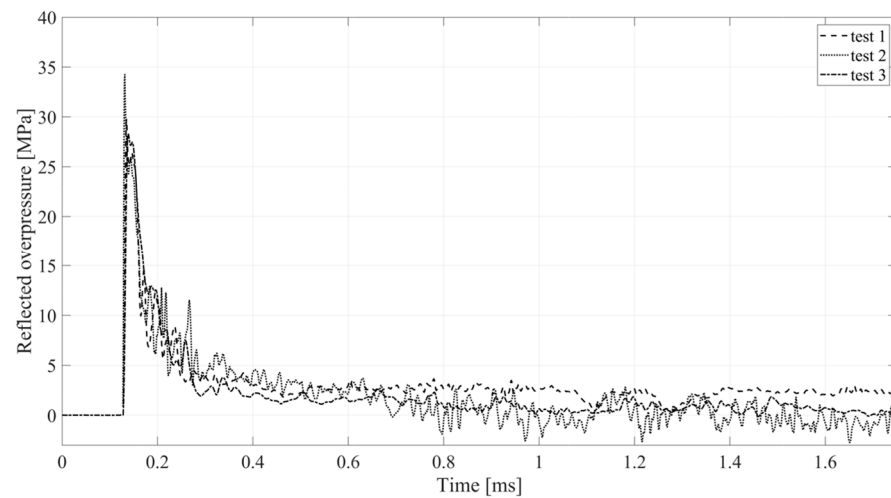


Figure 9. Reflected overpressure–time signals from the column sensor for a charge of 20 g of C4 for three different tests.

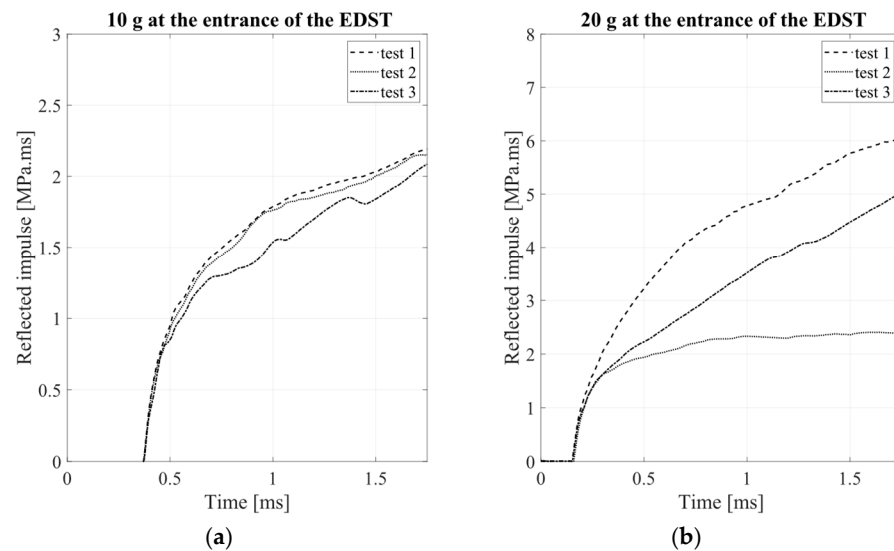


Figure 10. Reflected impulse–time signals from the column sensor for a charge of 10 g of C4 (a) and a charge of 20 g of C4 (b) for three different tests.

3.2. Blast Response of RC Columns

3.2.1. Displacement–Time Histories Using DIC Technique

Three RC columns are subjected to a blast loading generated by 30 g of C4 placed at the entrance of the EDST. The DIC technique allows the determination of the out-of-plane displacement field of the column within the area of interest. This displacement field is extracted from the DIC measurements for different time frames as shown in Figure 11. For comparison purposes, the focus will be on the out-of-plane displacement time histories of the positions D1, D2 and D3.

Figure 12 shows the out-of-plane displacement–time histories of the columns under blast loading. These results are extracted using the DIC technique. An average maximum displacement of 6.6 ± 0.4 mm, 6.8 ± 0.4 mm and 6 ± 0.4 mm is recorded at positions D1, D2 and D3, respectively. The small difference in the peak displacement at positions D1 and D3 is due to the asymmetry in the boundary conditions as shown in Figure 2. The permanent displacements are too small to be measured physically and will be determined numerically.

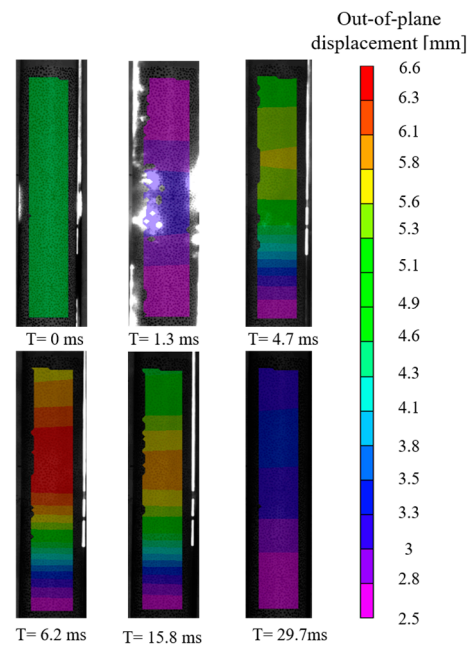


Figure 11. Out-of-plane displacement in the zone of interest (test n°2).

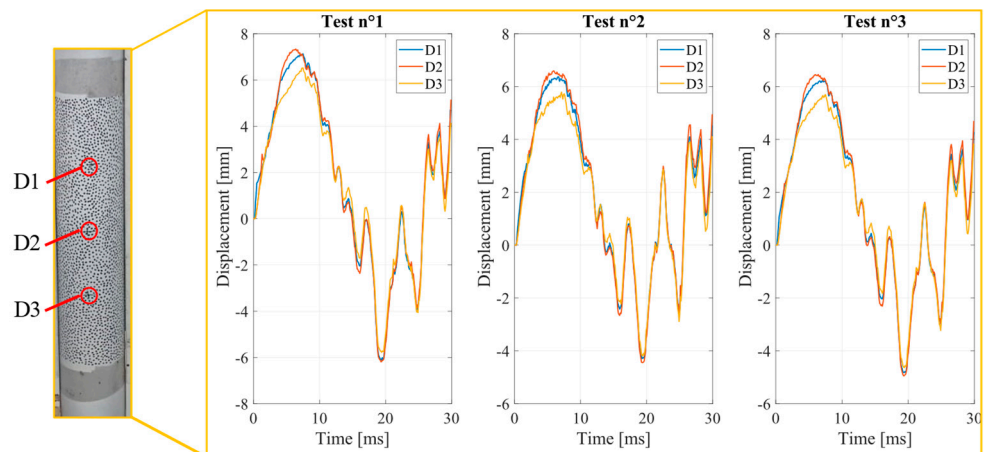


Figure 12. Displacement–time histories at the points D1, D2 and D3 using DIC.

3.2.2. Displacement–Time Histories Using LVDTs

The application of the DIC technique fails to accurately capture displacements over time within the area of interest when detonating a 50 g of C4 at the entrance of the EDST. This limitation arises due to the substantial formation of a fireball and smoke that obstructs the view between the column and the two cameras. Consequently, for the case of 50 g of C4, punctual displacement measurements are recorded using LVDTs. The experimental data at position D2 for test 6 and at position D3 for test n°4, test n°5 and test n°6 were not recorded due to LVDTs malfunction. Furthermore, the LVDTs detached from the tested columns after the first rebound phase due to the formation of cracks around the fixation points.

It can be seen from Figure 13 that the maximum displacement of 12.6 mm and 12.4 ± 0.3 mm is recorded at positions D2 and D1, respectively. An increase of 185% in mid-span displacement (i.e., position D2) is observed when increasing the explosive mass from 30 to 50 g.

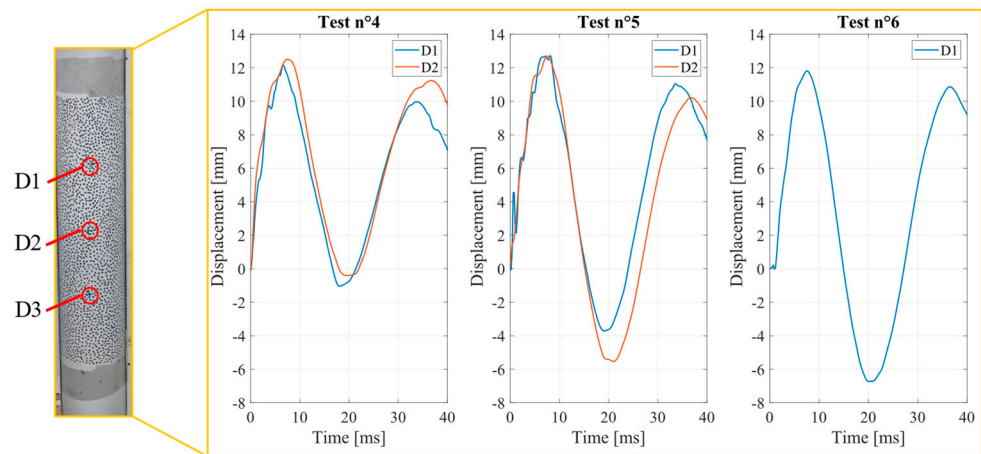


Figure 13. Displacement–time histories at points D1 and D2 using LVDTs.

3.2.3. Damage Pattern

As shown in Figure 14, hairline cracks, which are indicated using a red marker, appear in all of the loaded columns. When comparing the set of columns in Figure 14a,b, it can be seen that as the charge mass increases, the damage incurred to the test specimens increases. On the backside of the columns subjected to 30 g of C4, an average of six thin flexural cracks is observed in the central region. The average number of cracks rises to fifteen for a 50 g C4 loading. Moreover, the distribution of flexural cracks in this case spans the entire height of the column.

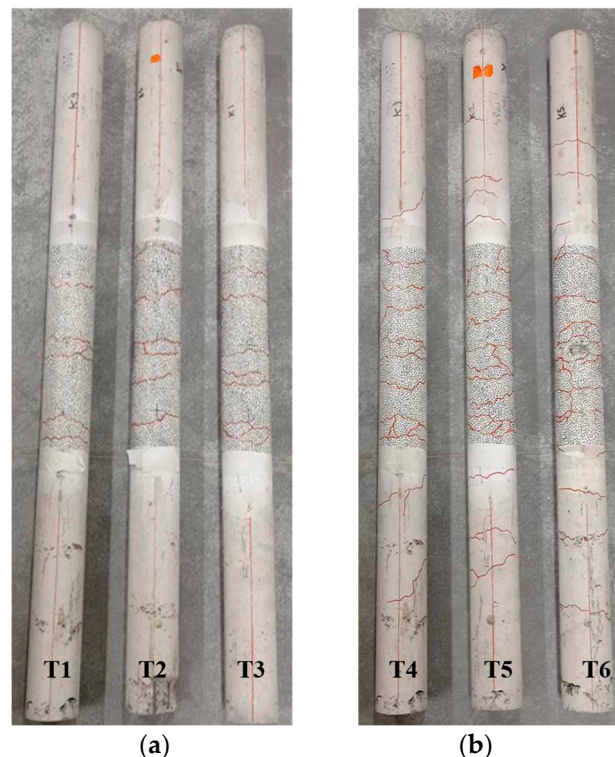


Figure 14. Post-test crack indication on the blast-loaded columns using a red marker under (a) 30 g (test n°1, test n°2 and test n°3) and (b) 50g (test n°4, test n°5 and test n°6).

The DIC technique also allows us to quantify the damage pattern of the blast-loaded RC column. As an example, the column of test n°2 is selected. Figure 15 shows the distribution of the cracks on the selected specimen. The first crack emerges at the mid-span of the column at 0.8 ms. At 0.9 ms, two additional cracks appear. At 6.2 ms, the RC column

reaches the maximum displacement with three cracks continuing to propagate. Next, the RC column returns to its initial position and the cracks gradually close at 14.6 ms, as shown in Figure 15. Two more cracks appear at 29.7 ms.

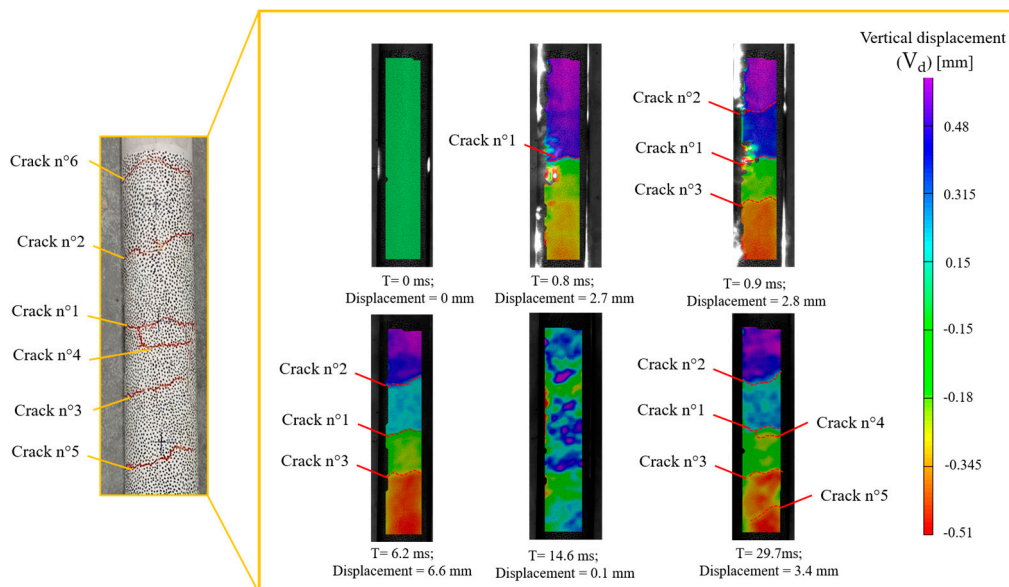


Figure 15. Distribution of the cracks on the RC column (test n°2) using the DIC technique.

In Figure 16a, the distribution of cracks within the area of interest is indicated after a post-mortem analysis of the blast-loaded RC column. Six cracks are highlighted in red and their spacing is measured. In Figure 16b, the spatial derivative of the vertical displacement V_d is plotted as a function of the coordinate Z . Other than crack n°6, situated out of the area of interest, the position of the five cracks along the Z axis is identified at -164.6 mm, -78.6 mm, -22.6 mm, 1.4 mm and 91.4 mm, respectively.

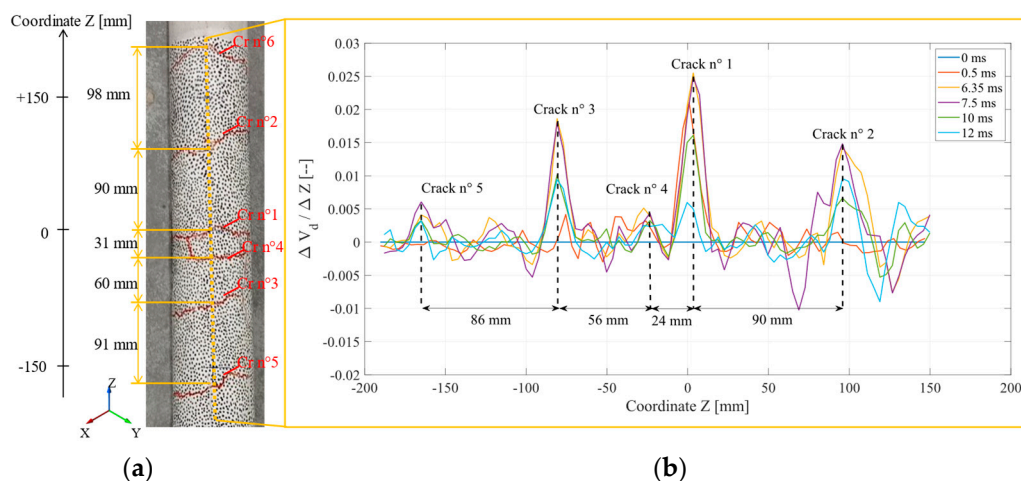


Figure 16. Identification of the cracks on the central line of the RC column (test n°2) using DIC.

To evaluate the damage observed in the RC columns, two parameters can be taken into account according to UFC-3-340-02 [4]. The first parameter, i.e., the support rotation (θ), refers to the angle between the vertical line and the line connecting the support point to the location of maximum deflection. The second parameter, i.e., the maximum deflection (D_{max}), represents the highest recorded displacement observed at the mid-span of the RC column. The classification of damage intensity for RC columns relies on these two

parameters. The classification includes three levels: superficial damage ($\theta < 1^\circ$), moderate damage ($1^\circ \leq \theta < 2^\circ$) and heavy damage ($2^\circ \leq \theta$).

A good agreement is found between the damage seen in the experimental results and the damage based on UFC-3-340-02.

Table 2 reports these two parameters, as well as the damage levels of the RC column after the explosion.

Table 2. Experimental results of the blast-loaded RC columns.

Test n°	Charge Mass [g]	D_{\max} [mm]	D_{mean} [mm]	Support Rotation θ [°]	UFC 3-340-02 Response Limit	Failure Model
1	30	7.3	6.8	0.6	Superficial damage	Multiple thin flexural cracks on the non-loaded side focusing on the central area.
2		6.6				
3		6.5				
4	50	12.5	12.6	1.1	Moderate damage	Deep flexural cracks on the non-loaded side along the height of the column.
5		12.7				
6		--				

4. Numerical Modeling

4.1. Finite Element Approach

The RC column and its motion under the blast load are modeled using a Lagrangian formulation. A schematic representation of the RC column is shown in Figure 17. A three-dimensional (3-D) finite element model simulates the RC column. The analysis is conducted using the LS-DYNA R10 explicit solver. Eight-node constant stress solid elements with one-point quadrature integration are adopted to model the concrete, while a two-node Hughes–Liu beam element with 2×2 Gauss quadrature integration is chosen for the steel reinforcements. The wooden plates and the steel supports are discretized into eight-node solid elements with constant stress solid element formulation. In this study, the wooden plates and the steel supports are constrained to prevent any translational movement (x and y directions). The bottom face of the column is also fixed to prevent vertical motion in the z direction. The multi-material arbitrary Lagrange–Eulerian (MM-ALE) formulation is adopted for modeling the air and explosive domains.

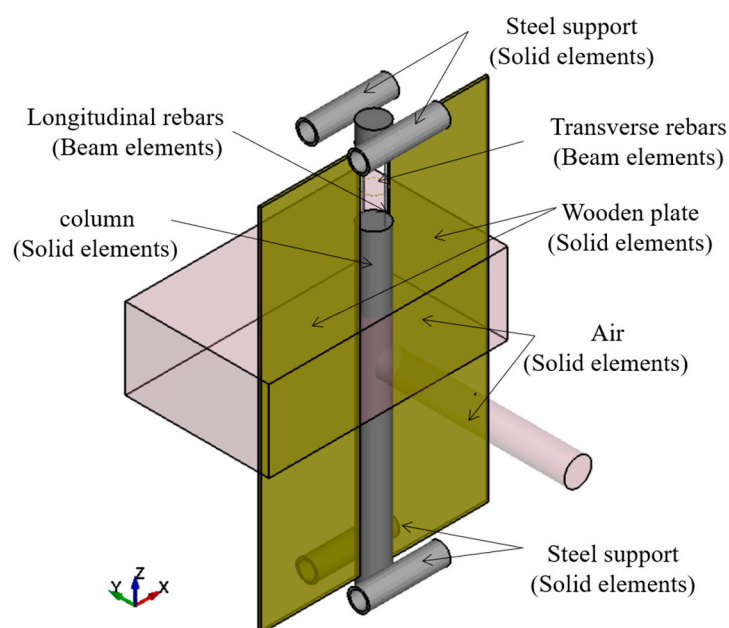


Figure 17. Finite element model of the laboratory-scale RC column subjected to localized blast loading.

4.2. Air and Explosion Modeling

The numerical simulation, using the MM-ALE method, is divided into two components: the C4 explosive charge and the surrounding air. This simulation is further categorized into a 2D axially symmetric model and a 3D ALE model, illustrated in Figure 20a and Figure 20b, respectively. Numerical tracers are positioned at 2 mm to monitor pressure–time histories. The goal is to identify the optimal termination time before it reaches the tube’s exit. The MMALE formulation was used to model both the air and explosive domains. The explosive charge is defined by the INITIAL-VOLUME-FRACTION keyword. For the case of the explosive material, the MAT-HIGH-EXPLOSIVE-BURN is adopted along with an EOS. EOS-JONES-WILKINS-LEE which governs the hydrodynamic behavior of the explosive is selected. The inputs A , B , R_1 , R_2 , ω and E , included in Equation (1), are defined based on the explosive material.

$$P = A \left(1 - \frac{w}{R_1 V} \right) \exp^{-R_1 V} + B \left(1 - \frac{w}{R_2 V} \right) \exp^{-R_2 V} + \frac{\omega E}{V} \quad (1)$$

Table 3 displays the variables of C4 which are taken from [54].

Table 3. C4 material properties and EOS parameters.

EOS-JWL		MAT-HIGH-EXPLOSIVE-BURN						
A [GPa]	B [GPa]	R_1	R_2	ω	E [kJ.kg ⁻¹]	ρ [kg/m ³]	P_{cj} [GPa]	D_v [m/s]
609.77	12.95	4.5	1.4	0.25	9	1601	28	8193

In this approach, the air domain is designated as MAT_NULL, enabling the equation of state (EOS) to be incorporated without the need to compute deviatoric stresses [55].

The EOS-LINEAR-POLYNOMIAL defines the air domain and allows it to act like a fluid. The pressure P in the air element is calculated using Equation (2).

$$P = C_0 + C_1 \mu + C_2 \mu^2 + C_3 \mu^3 + (C_4 + C_5 \mu + C_6 \mu^2) E_0 \quad (2)$$

where C_0 , C_1 , C_2 , C_3 , C_4 , C_5 and C_6 are coefficients of the polynomial equation. The pressure is calculated as a function of the specific internal energy of air E_0 , and variable $\mu = (\rho / \rho_0) - 1$, where ρ and ρ_0 are the current and initial densities, respectively. The initial relative volume is set as $V_0 = 1$. The set of parameters assumed for air is summarized in Table 4.

Table 4. Air material properties and EOS parameters.

EOS-LINEAR-POLYNOMIAL					MAT-NULL				
C_0	C_1	C_3	C_4	C_5	E_0 [kJ.kg ⁻¹]	v_0	ρ_0 [kg/m ³]	P_c [GPa]	V_0 [-]
0	0	0	0.4	0.4	0.2534	1	1.29	0	1

4.3. RC Column Modeling

4.3.1. Concrete Modeling

Material type 072_Rel3 (*MAT_CONCRETE DAMAGE REL3) is used to model the concrete parts. This model, which is the third release of the Karagozian and Case (K&C) model, has been widely used to represent concrete behavior in RC structural elements subjected to blast loading [10,56]. The model uses a plasticity-based methodology featuring three shear failure surfaces and incorporates the capacity to accommodate strain rate effects. This model includes non-linear hardening and softening, shear dilation and the confinement effect [57]. To prevent numerical instabilities arising from excessively distorted elements, these elements are eroded when the principal maximum strain is equal to 0.1

introduced in the *MAT_ADD_EROSION card [58]. The input parameters for the concrete model are presented in Table 5.

Table 5. Material properties for the MAT_072 concrete model.

Parameter	Value
Mass density (kg/m ³)	2255
Uniaxial compressive strength (MPa)	32
Poisson's ratio	0.3

In the MAT_072 concrete model, the expressions presented in Comité Euro-international du Béton CEB [59] are used to account for dynamic loading effects for concrete in compression:

$$DIF_c = \frac{f_c}{f_{cs}} = \begin{cases} \left(\frac{\dot{\epsilon}}{\dot{\epsilon}_s}\right)^{1.026\alpha}, & \dot{\epsilon} \leq 30 \text{ s}^{-1} \\ \gamma \left(\frac{\dot{\epsilon}}{\dot{\epsilon}_s}\right)^{1/3}, & \dot{\epsilon} > 30 \text{ s}^{-1} \end{cases} \quad (3)$$

where $\dot{\epsilon}_s = 30 * 10^{-6} \text{ s}^{-1}$ is the static strain rate, $\log \gamma = 6.156\alpha - 2$, $\alpha = \frac{1}{5+9(f_{cs}/10)}$, f_c is the compressive strength for a given strain rate and f_{cs} is the quasi-static compressive strength.

For concrete in tension, Malvar and Crawford [60] proposed the following expressions:

$$DIF_t = \frac{f_t}{f_{ts}} = \begin{cases} \left(\frac{\dot{\epsilon}}{\dot{\epsilon}_s}\right)^\delta, & \dot{\epsilon} \leq 1 \text{ s}^{-1} \\ \beta \left(\frac{\dot{\epsilon}}{\dot{\epsilon}_s}\right)^{1/3}, & \dot{\epsilon} > 1 \text{ s}^{-1} \end{cases} \quad (4)$$

where $\dot{\epsilon}_s = 10^{-6} \text{ s}^{-1}$ is the static strain rate, and $\beta = 10^{7.11\delta-2.33}$; $\delta = \frac{1}{10+8(f_{ts}/10)}$. f_t is the tensile strength for a given strain rate, and f_{ts} is the quasi-static tensile strength.

The curves shown in Figure 18 are implemented in the constitutive model.

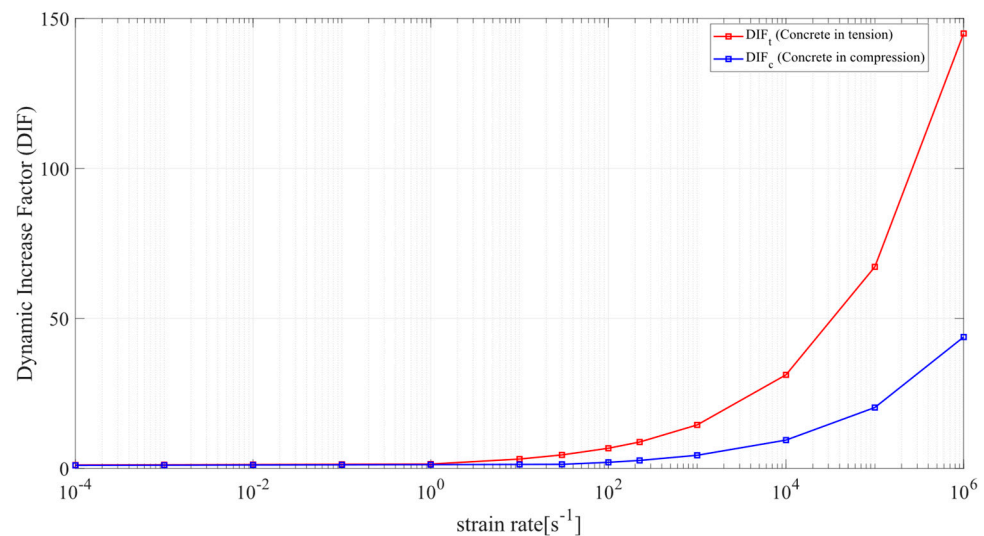


Figure 18. DIF as a function of the strain rate for the case of concrete.

4.3.2. Reinforcement Modeling

Material type 024 (PIECEWISE_LINEAR_PLASTICITY) includes elastoplastic behavior, allowing the specification of an engineering stress–strain curve for a designated material. Additionally, this model uses an arbitrary strain rate curve or the Cowper–Symonds rate enhancement feature. Detailed input parameters of this model are provided in Table 6.

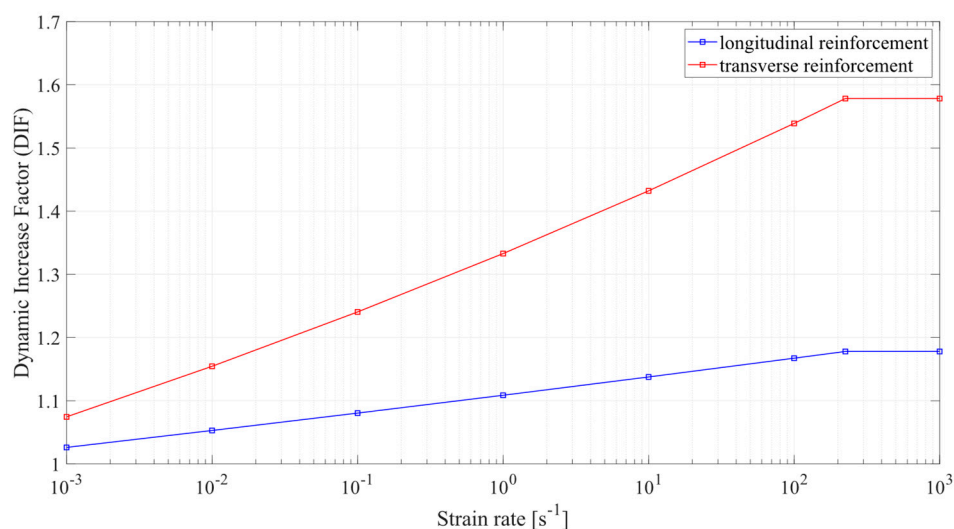
Table 6. Static material parameters for MAT_024 constitutive model.

Parameter	Longitudinal Steel Reinforcement	Transverse Steel Reinforcement
Mass density (kg/m ³)	7800	7800
Yield strength (MPa)	650	443
Young's modulus (GPa)	210	199
Poisson's ratio	0.33	0.33
Failure strain	6.4%	11.3%

Due to the sensitivity of most structural materials to high loading rates, it is crucial to increase the mechanical properties of steel reinforcement under highly dynamic loading conditions. This dynamic increase factor (*DIF*) quantifies the ratio of dynamic to static yield stress. In this work, the *DIF* of the steel bars is as follows [61]:

$$DIF = \left(\frac{\dot{\epsilon}}{\dot{\epsilon}_s} \right)^\alpha; \alpha = 0.074 - 0.04 \frac{f_y}{414} \quad (5)$$

where $\dot{\epsilon}_s = 10^{-4} \text{ s}^{-1}$ represents the static loading, $\dot{\epsilon}$ is the strain rate of reinforcement and f_y (yield strength) is expressed in MPa. This formula is valid for strain rates between 10^{-4} s^{-1} and 225 s^{-1} . The curve shown in Figure 19 is introduced in the constitutive model.

**Figure 19.** DIF as a function of the strain rate for the case of steel reinforcement.

4.3.3. Boundary Conditions

The steel supports are defined using material type 024 (PIECEWISE_LINEAR_PLASTICITY) as proposed in [56]. Detailed input parameters of the steel support are provided in Table 7. To avoid unwanted damage near the supports and to prevent penetration between the steel supports and the concrete surface during the explosion, a command 'Automatic-Surface-to-Surface' is applied between the supports and the specimen. The selected values for the static and the kinematic friction coefficients are equal to 0.6 and 0.5, respectively [62–64].

A perfect bond between the steel reinforcement and the concrete is assumed [65]. The fluid–structure interaction (FSI) between the blast wave and the RC column is implemented by the Constrained-Lagrange-In-Solid (CLIS) keyword with the fluid–structure coupling method n°5 (CTYPE 5). The implemented CLIS parameters are 5, 5, 3, 5 and 2 for the number of coupling points distributed over each coupled Lagrangian surface segment (NQAD), CTYPE, coupling direction (DIREC), penalty factor (PFAC) and leakage control (ILEAK), respectively.

Table 7. Material parameters for MAT_024 constitutive model for steel support.

Parameter	Value
Mass density (kg/m ³)	7800
Yield strength (MPa)	600
Young's modulus (GPa)	210
Poisson's ratio	0.33
Failure strain	6%

4.3.4. Mesh Convergence

For the 2D numerical model, a mesh convergence study is conducted with five finite element sizes, namely, 0.5 mm, 2 mm, 4 mm and 8 mm. Findings indicate convergence is achieved at a mesh size of 1 mm. This optimal size aligns with the recommendation provided by Schwer [66]. The first simulation is terminated before the arrival of the traveling blast wave within 2 mm from the exit of the shock tube. The subsequent simulation begins with a larger 3D-ALE domain of a 2 mm minimum element size.

The size of the 3D-ALE domain is chosen as 440 mm × 530 mm × 300 mm, excluding the air domain representing the EDST. This size is selected to prevent the reflection of the blast wave when reaching the boundaries of the air domain [55]. To optimize the balance between result precision and computational efficiency, a 10 mm mesh configuration is selected for the RC column [45].

4.4. Comparison between the Full and Half Model

Considering (a) the spherical shape of the explosive charge, (b) the circular configuration of the EDST's cross-sectional area and (c) the axisymmetric nature of the shock tube, a 2D axisymmetric, purely Eulerian model was constructed as seen in Figure 20a. Due to the positioning of the explosive charge at the entrance of the EDST, a considerable amount of energy is expected to be discharged there. Therefore, an air volume with a length of 100 mm is added at the inlet of the tube as shown in Figure 20a. A second volume is added to the ALE domain in which the RC column is inserted as shown in Figure 20b. This chained simulation, which is a 2D to 3D mapping technique within LS-DYNA, is implemented to accurately predict the blast wave detonation and propagation and the interaction with the RC column.

Before proceeding, a comparison is made between the dynamic response of a full and a half model. The half model will be used for the parametric study. Displacement–time histories at the positions D1, D2 and D3 are shown in Figure 21. The results emphasize that the reduction in size of the model and the boundary conditions do not affect the blast response of the RC column.

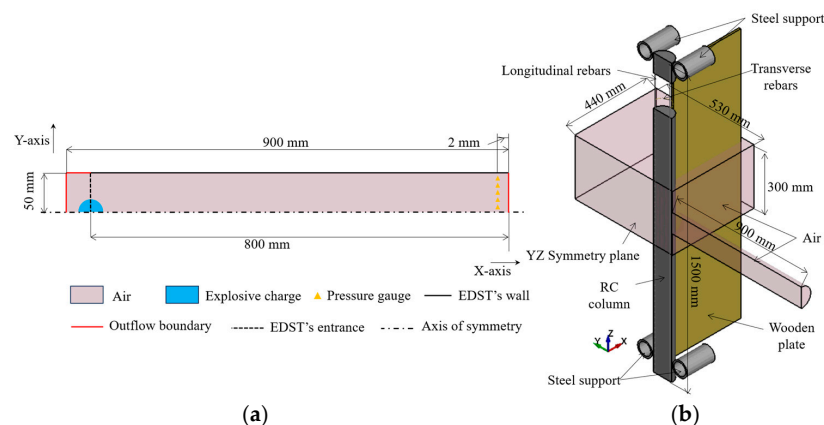


Figure 20. Finite element model of (a) localized blast loading generated by an EDST and (b) half model of RC column with the plane of symmetry.

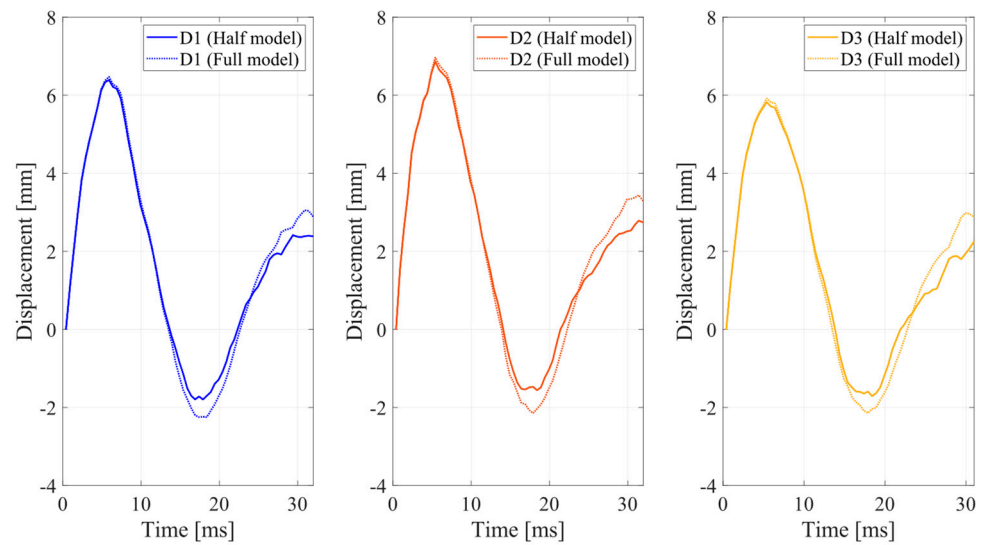


Figure 21. Comparison of the displacement–time histories at the positions D1, D2 and D3 of the full and half models.

5. Validation of Finite Element Modeling

5.1. Blast Loading

Figures 22 and 23 show the pressure–time histories from the experiments in comparison to the results of the numerical simulation. The computed reflected peak pressures are equal to 15.3 MPa and 32.3 MPa for charges of 10 g and 20 g of C4.

In Figure 24, the numerical reflected impulses are 2.1 MPa.ms and 3.8 MPa.ms for the 10 g and 20 g explosive charges, respectively. The relative difference in the peak reflected pressures between the finite element model and the average measured data is equal to 1.3% and 6.6% for charges of 10 g and 20 g, respectively. Similarly, the relative difference in the peak reflected impulses is 7.3% and 18.5%.

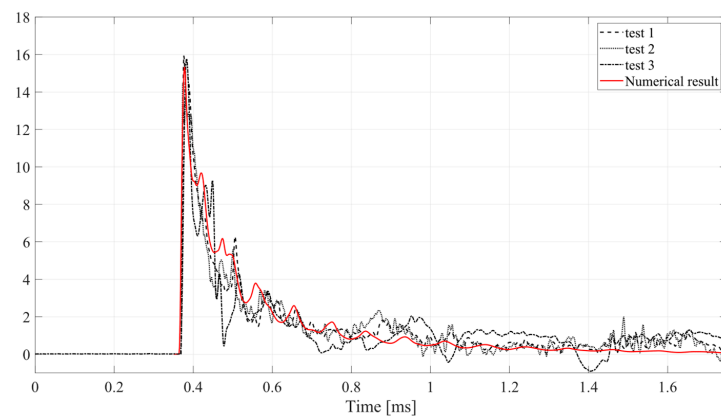


Figure 22. Comparison of the reflected overpressure–time histories of the column sensor for a charge of 10 g of C4.

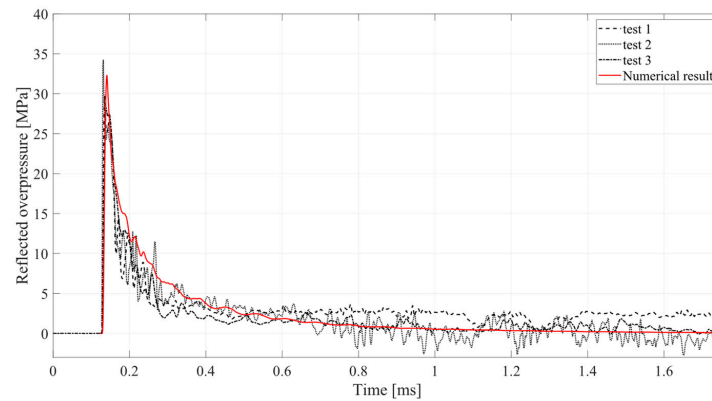


Figure 23. Comparison of the reflected overpressure–time histories of the column sensor for a charge of 20 g of C4.

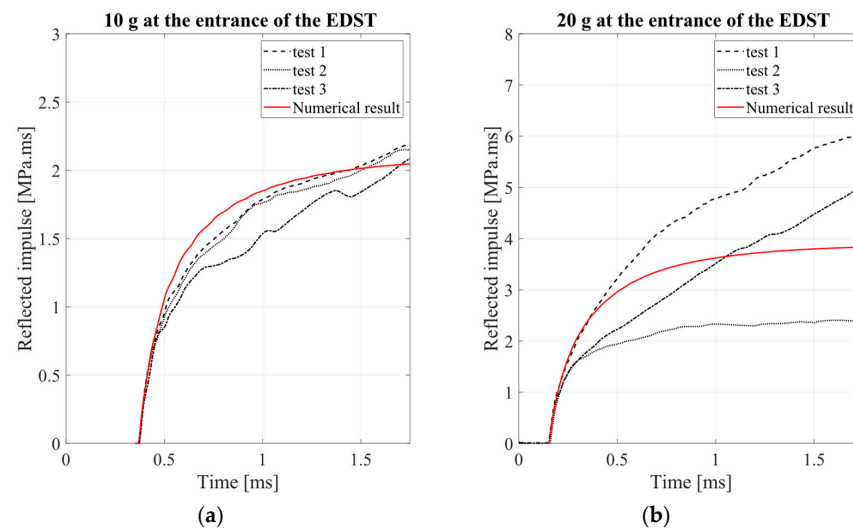


Figure 24. Comparison of the reflected impulse–time histories of the column sensor for a charge of 10 g of C4 (a) and 20 g of C4 (b).

5.2. RC Column Behavior

5.2.1. Displacement–Time Histories

DIC is used to obtain the out-of-plane displacement of the RC column at positions D1, D2 and D3. For the case of 30 g of C4, only the inbound phase is recorded during the experiments. However, the numerical results give more details about the blast response during the inbound and rebound phases of the specimens. A maximum displacement of 6.6 mm, 6.9 mm and 5.8 mm is measured at D1, D2 and D3, respectively. A relative difference of 3.3%, 1.5% and 1.5% is found at D1, D2 and D3, as shown in Figure 25. For the case of 50 g of C4, a maximum displacement of 12.7 mm and 13.3 mm is measured at D1 and D2. A relative difference of 5.6% and 1.6% are found at D1 and D2 as seen in Figure 26.

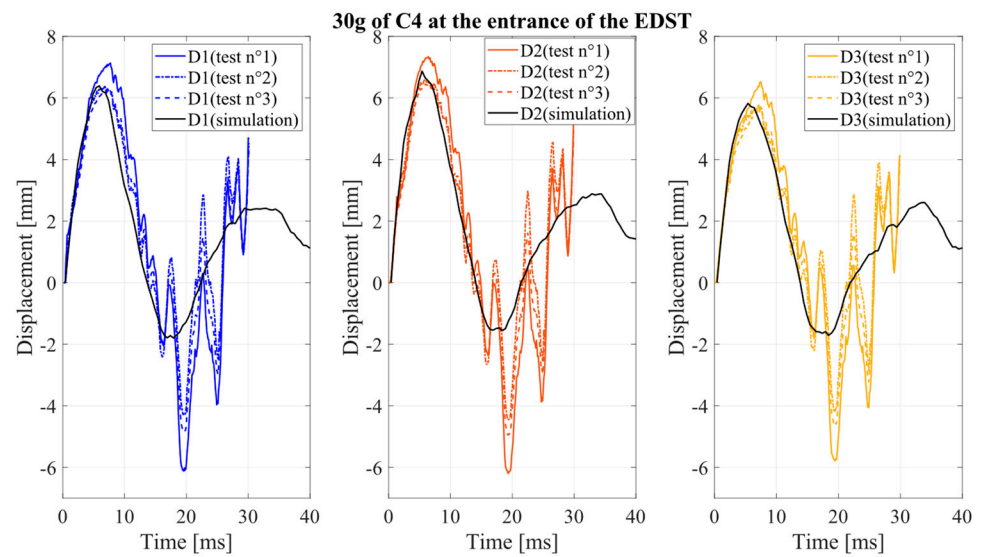


Figure 25. Displacement–time histories at positions D1, D2 and D3 for 30 g of C4.

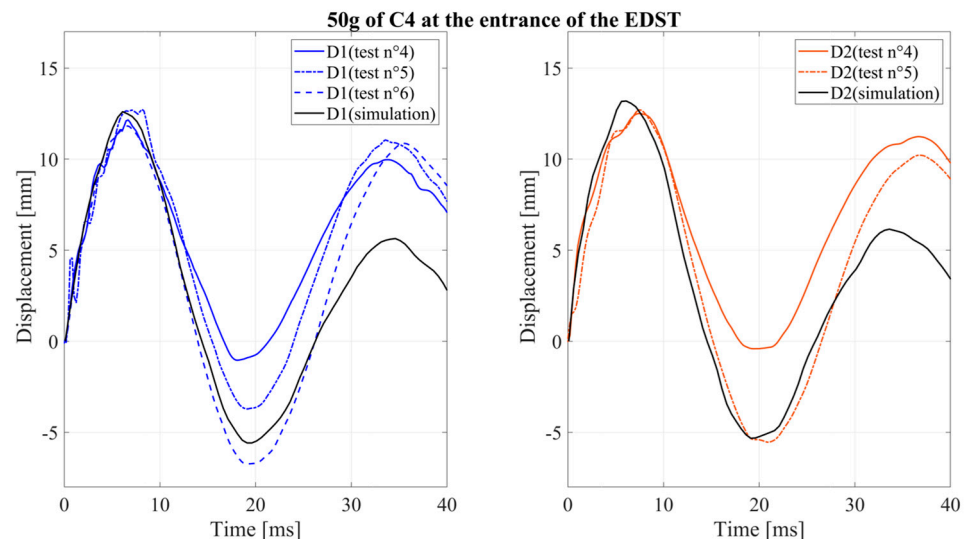


Figure 26. Displacement–time histories at positions D1 and D2 for 50 g of C4.

5.2.2. Crack Pattern

The damage of the RC columns is shown in Figure 27 according to the equivalent plastic strain using a normalized scale of 0 to 2. A value of 1 indicates that the concrete has just reached its peak strength, and a value between 1 and 2 shows that the concrete has exceeded its peak strength and is in the softening stage. Comparing the crack pattern of the numerical results for 30 g of C4 with the experimental results shows that the cracks (represented in red) are concentrated around the central area of the RC column. However, the numerical model also shows some cracks at one-third and two-third of the height of the column. For 50 g of C4, the crack pattern predicted with the numerical model corresponds well with the experimental results. The assessment of damage incurred by the blast loading in the different scenarios is also performed through an examination of the total internal energy within the respective columns. The total internal energy of a column is defined as the sum of the internal energy of the reinforcement bars and the concrete material [65]. The total energy is equal to 78 J and 212 J under 30 g and 50 g, respectively as shown in Figure 28. The internal energy of the steel reinforcement is observed to range between 22% and 34% of the column's internal energy for the two cases.

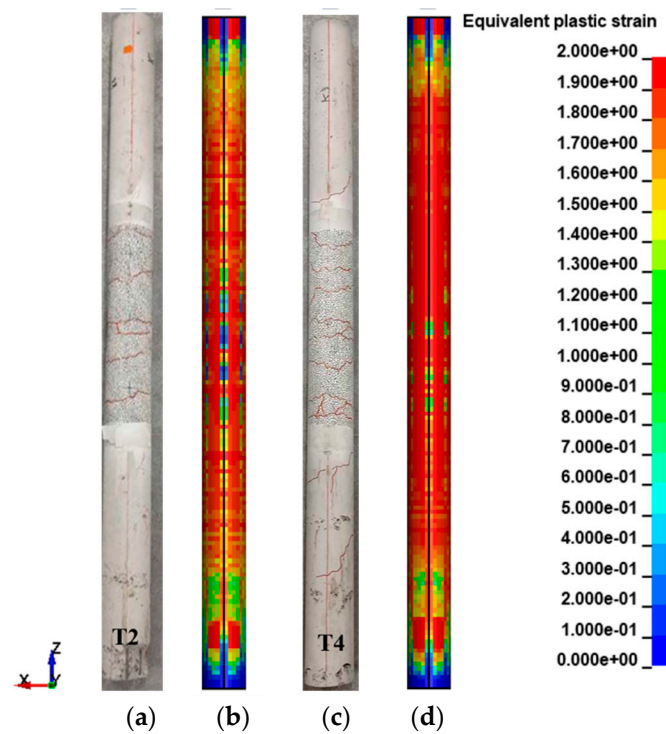


Figure 27. Equivalent plastic strain for the case of 30 g (a,b) and 50 g (c,d).

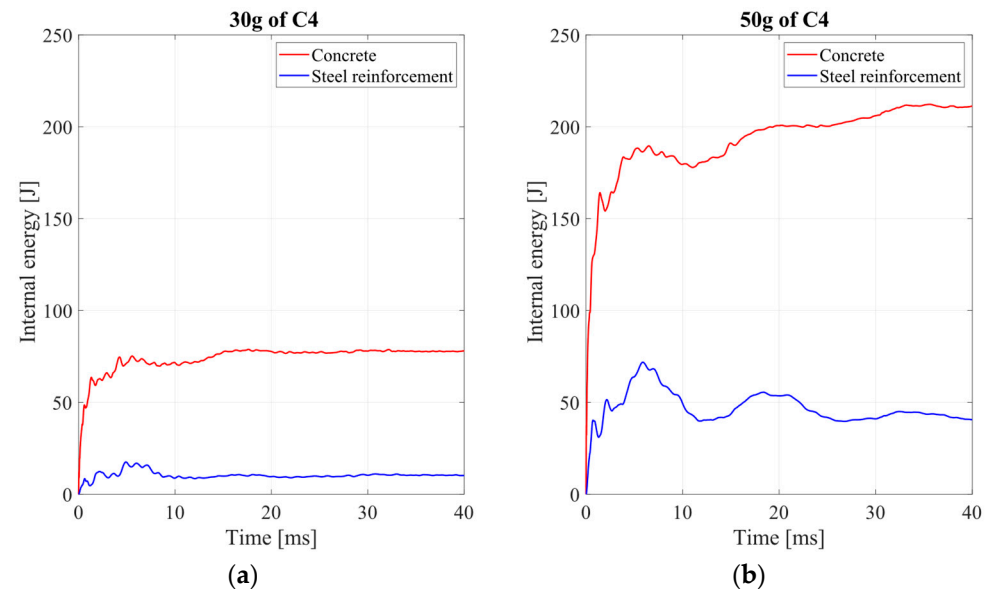


Figure 28. Internal energy of the RC columns as a function of time for the case of (a) 30 g of C4 and (b) 50 of C4.

6. Sensitivity Analysis

6.1. Gray Method

In the gray correlation method, the correlation coefficient is used to indicate the extent of association between variables, with values ranging from 0 to 1. A coefficient closer to 1 signifies a higher degree of correlation, while closer to 0 indicates a lower degree of correlation [42]. The specific calculation steps for this method are outlined as follows:

- (1) Selection of the sequence matrix

The parameters affecting the mid-span displacement and internal energy of the RC column are as follows:

- Diameter of longitudinal bar φ_L ;
- Number of longitudinal bars n_L ;
- Diameter of the tie φ_t ;
- Spacing of the transverse bars s_t ;
- Strength of concrete s_c ;
- Mass of the explosive charge at the entrance of the EDST m_e ;
- Load eccentricity h_r ;

These parameters are selected as the influence parameter sequence $X = (X_1 X_2 \dots X_n)^T$. The corresponding mid-span displacement total internal energy are represented as the parent sequence $Y = (Y_1 Y_2 \dots Y_n)^T$ and $Z = (Z_1 Z_2 \dots Z_n)^T$. Each parameter of series X , Y and Z has i and j values and a matrix form as shown herein:

$$X = \begin{pmatrix} X_1 \\ X_2 \\ \vdots \\ X_i \end{pmatrix} = \begin{pmatrix} X_{11} & X_{12} & \cdots & X_{1j} \\ X_{21} & X_{22} & \cdots & X_{2j} \\ \vdots & \vdots & \ddots & \vdots \\ X_{i1} & X_{i2} & \cdots & X_{ij} \end{pmatrix} \quad (6)$$

$$Y = \begin{pmatrix} Y_1 \\ Y_2 \\ \vdots \\ Y_i \end{pmatrix} = \begin{pmatrix} Y_{11} & Y_{12} & \cdots & Y_{1j} \\ Y_{21} & Y_{22} & \cdots & Y_{2j} \\ \vdots & \vdots & \ddots & \vdots \\ Y_{i1} & Y_{i2} & \cdots & Y_{ij} \end{pmatrix} \quad (7)$$

$$Z = \begin{pmatrix} Z_1 \\ Z_2 \\ \vdots \\ Z_i \end{pmatrix} = \begin{pmatrix} Z_{11} & Z_{12} & \cdots & Z_{1j} \\ Z_{21} & Z_{22} & \cdots & Z_{2j} \\ \vdots & \vdots & \ddots & \vdots \\ Z_{i1} & Z_{i2} & \cdots & Z_{ij} \end{pmatrix} \quad (8)$$

- (2) Dimensionless treatment of the matrix X , Y and Z

Matrix X is transformed based on Equation (9) for the purpose to render it dimensionless [41].

$$X'_i = \frac{X_i - \min(X_i)}{\max(X_i) - \min(X_i)} \quad (9)$$

where X'_i is dimensionless data of i th simulation. Similarly, matrices Y and Z are transformed using the same equation.

- (3) Difference sequence matrix

The difference sequence matrix Δ_{X-Y} is calculated following Equation (10). The maximum and minimum values are then determined using Equation (11).

$$\Delta_{X-Y}^{ij} = |Y'_{ij} - X'_{ij}|; \quad \Delta_{X-Z}^{ij} = |Z'_{ij} - X'_{ij}|; \quad (10)$$

$$\begin{cases} \Delta_{X-Y}^{max} = \max(\Delta_{X-Y}^{ij}) \\ \Delta_{X-Y}^{min} = \min(\Delta_{X-Y}^{ij}) \end{cases}; \quad \begin{cases} \Delta_{X-Z}^{max} = \max(\Delta_{X-Z}^{ij}) \\ \Delta_{X-Z}^{min} = \min(\Delta_{X-Z}^{ij}) \end{cases}; \quad (11)$$

- (4) Gray correlation coefficient

The gray relational coefficient is computed using Equation (12):

$$\delta_{X-Y}^{ij} = \frac{\Delta_{X-Y}^{min} - \zeta \Delta_{X-Y}^{max}}{\Delta_{X-Y}^{ij} - \zeta \Delta_{X-Y}^{max}}; \quad \delta_{X-Z}^{ij} = \frac{\Delta_{X-Z}^{min} - \zeta \Delta_{X-Z}^{max}}{\Delta_{X-Z}^{ij} - \zeta \Delta_{X-Z}^{max}} \quad (12)$$

where δ_{X-Y}^{ij} and δ_{X-Z}^{ij} are the gray relational coefficient, and ζ is the identification coefficient that varies between 0 and 1, and it is generally chosen as 0.5 [35,42,67].

(5) Determination of the gray relational grade

Finally, the gray relational grade χ is calculated using Equation (13):

$$\chi_{X-Y}^i = \frac{1}{n} \sum_{i=1}^n \delta_{X-Y}^i; \chi_{X-Z}^i = \frac{1}{n} \sum_{i=1}^n \delta_{X-Z}^i \tag{13}$$

where χ_{X-Y}^i and χ_{X-Z}^i are the gray relational grades of the i th simulation, and n is the total number of variations.

The correlation value falls within the range of [0, 1], with higher values indicating greater sensitivity of the influencing parameter to the reference sequence.

6.2. Study of the Variables

In this study, the parameters indicated in Section 6.1 are varied in order to determinate their influence on the dynamic response of the RC column under localized blast loading as shown in Tables 8 and 9.

Table 8. Parametric study with respect to column and blast loading-related parameters.

FE Model	φ_L [mm]	n_L	φ_t [mm]	s_t [mm]	s_c [MPa]	m_e [g]	h_r
1	6–8–10–12	4	2	185	30	50	1
2	8	4–6–8–10	2	185	30	50	1
3	8	4	2–4–6–8	185	30	50	1
4	8	4	2	148–185–246–370	30	50	1
5	8	4	2	185	20–30–40–50	50	1
6	8	4	2	185	30	40–50–60–70	1
7	8	4	2	185	30	50	0.5–1–1.33–1.5

Table 9. Influence of the chosen parameters on the mid-span displacement and the internal energy of the RC column based on gray relational grade.

Mid-Span Displacement of the RC Column						
φ_L [mm]	n_L	φ_t [mm]	s_t [mm]	s_c [MPa]	m_e [g]	h_r
0.51	0.55	0.41	0.86	0.49	0.78	0.69
Internal Energy of the RC column						
φ_L [mm]	n_L	φ_t [mm]	s_t [mm]	s_c [MPa]	m_e [g]	h_r
0.47	0.53	0.46	0.97	0.49	0.81	0.56

Using the parameter values detailed in Table 8, the gray relation degree is computed:

$$X = \begin{pmatrix} X_1 \\ X_2 \\ X_3 \\ X_4 \\ X_5 \\ X_6 \\ X_7 \end{pmatrix} = \begin{pmatrix} 6 & 8 & 10 & 12 \\ 4 & 6 & 8 & 10 \\ 2 & 4 & 6 & 8 \\ 148 & 185 & 246 & 370 \\ 20 & 30 & 40 & 50 \\ 40 & 50 & 60 & 70 \\ 0.5 & 1 & 1.33 & 1.5 \end{pmatrix} \tag{14}$$

$$Y = \begin{pmatrix} Y_1 \\ Y_2 \\ Y_3 \\ Y_4 \\ Y_5 \\ Y_6 \\ Y_7 \end{pmatrix} = \begin{pmatrix} 13.4 & 10 & 8.7 & 7.5 \\ 10 & 7.9 & 7.8 & 6.9 \\ 10 & 9.7 & 8.4 & 8.1 \\ 9.8 & 10 & 10.3 & 13.3 \\ 10.3 & 10 & 9.8 & 9.4 \\ 9.9 & 10 & 11.7 & 15.7 \\ 5.8 & 10 & 8.2 & 8.4 \end{pmatrix} \tag{15}$$

$$Z = \begin{pmatrix} Z_1 \\ Z_2 \\ Z_3 \\ Z_4 \\ Z_5 \\ Z_6 \\ Z_7 \end{pmatrix} = \begin{pmatrix} 128 & 122 & 116 & 108 \\ 122 & 111 & 108 & 90.1 \\ 122 & 119 & 116 & 114 \\ 121 & 122 & 124 & 127 \\ 131 & 122 & 118 & 112 \\ 117 & 122 & 154 & 227 \\ 144 & 122 & 117 & 142 \end{pmatrix} \quad (16)$$

The calculated difference sequence matrices Δ_{X-Y} and Δ_{X-Z} are shown below.

$$\Delta_{X-Y} = \begin{pmatrix} 1 & 0.09 & 0.46 & 1 \\ 1 & 0.01 & 0.38 & 1 \\ 1 & 0.51 & 0.51 & 1 \\ 0 & 0.11 & 0.3 & 0 \\ 1 & 0.33 & 0.22 & 1 \\ 0 & 0.32 & 0.36 & 0 \\ 0 & 0.52 & 0.21 & 0.38 \end{pmatrix}; \Delta_{X-Z} = \begin{pmatrix} 1 & 0.37 & 0.27 & 1 \\ 1 & 0.32 & 0.11 & 1 \\ 1 & 0.29 & 0.42 & 1 \\ 0 & 0 & 0.06 & 0 \\ 1 & 0.19 & 0.35 & 1 \\ 0 & 0.29 & 0.33 & 0 \\ 1 & 0.29 & 0.79 & 0.07 \end{pmatrix} \quad (17)$$

The correlation coefficient matrices δ_{X-Y} and δ_{X-Z} are detailed here:

$$\delta_{X-Y} = \begin{pmatrix} 0.33 & 0.85 & 0.52 & 0.33 \\ 0.33 & 0.98 & 0.57 & 0.33 \\ 0.33 & 0.5 & 0.5 & 0.33 \\ 1 & 0.82 & 0.63 & 1 \\ 0.33 & 0.6 & 0.69 & 0.33 \\ 1 & 0.61 & 0.58 & 1 \\ 1 & 0.49 & 0.7 & 0.57 \end{pmatrix}; \delta_{X-Z} = \begin{pmatrix} 0.33 & 0.58 & 0.65 & 0.33 \\ 0.33 & 0.61 & 0.83 & 0.33 \\ 0.33 & 0.63 & 0.55 & 0.33 \\ 1 & 1 & 0.9 & 1 \\ 0.33 & 0.72 & 0.59 & 0.33 \\ 1 & 0.63 & 0.60 & 1 \\ 0.33 & 0.63 & 0.39 & 0.87 \end{pmatrix} \quad (18)$$

The sensitivity analysis reveals that, in decreasing order of sensitivity, the mid-span displacement and total internal energy of the RC column are influenced by the following parameters as shown in Table 9:

- (1) Spacing of the transverse bars (s_t);
- (2) Mass of the explosive charge at the entrance of the EDST (m_e);
- (3) Load eccentricity (h_r);
- (4) Number of longitudinal bars (n_L);
- (5) Diameter of longitudinal bar (φ_L);
- (6) Strength of concrete (s_c);
- (7) Diameter of the tie (φ_t).

Wu et al. [35] used the gray relation method to assess the influence of various parameters on the dynamic response of square RC columns under a close-in explosion. It was shown that the spacing of the transverse bars (s_t) has the most important impact on the mid-span peak displacement of RC columns. Similar results are shown in this work for the case of circular RC columns under localized blast loading.

Adding to the parameters studied in [35], the influence of the load eccentricity is also investigated in this work.

7. Conclusions

This study introduces a novel approach for experimentally testing laboratory-scale RC columns under blast loading. The explicit LS-DYNA code is used for numerical simulation, and the obtained results are validated with respect to the experimental data. The established laboratory-scale approach allows for the evaluation of the blast response of circular RC columns, combining the use of the EDST as a blast loading tool and the DIC technique for detailed deformation measurement and failure estimation.

The following conclusions can be presented:

1. An increased explosive mass correlates with a higher damage level in the RC columns. The rotation-based damage assessment for the RC column subjected to an explosive mass of 30 g (tests n°1, 2, 3) reveals a classification of superficial damage, indicated by a support rotation (θ) of 0.6° . This contrasts with the damage level of the specimens (tests n°5, 6, 7) subjected to 50 g, which is categorized as moderate damage, as evidenced by a support rotation (θ) of 1.1° .
2. The crack pattern of the blast-loaded RC column is identified using the DIC measurements. Differentiation of the vertical displacement field yields the position of the different appeared cracks in the columns.
3. The FE model is able to reproduce the applied blast loading in terms of the reflected pressure and impulse. The relative difference in the peak reflected pressures between the finite element model and the average measured data is equal to 1.3% and 6.6% for charges of 10 g and 20 g, respectively. The relative difference in the peak reflected impulses is 7.3% and 18.5%.
4. The FE model allows us to uncover details about the deformation and failure characteristics of the RC columns under localized blast loading.
5. The FE model is capable of reproducing the dynamic response of the RC columns. The relative difference in the peak displacement at positions D1, D2 and D3 between the finite element model and the average measured data is equal to 3.3%, 1.5% and 1.5% for the case of 30 g of C4, respectively. For the case of 50 g, the relative difference in the peak displacement at positions D1 and D2 is equal to 5.6% and 1.6%, respectively.
6. The relative difference in the support rotation (θ) between the finite element model and the experimental results is equal to 6.7% and 5.6% for the case of 30 g and 50 g, respectively.
7. The crack pattern predicted with the numerical model corresponds well with the experimental results.
8. The sensitivity analysis reveals that, in decreasing order of sensitivity, the mid-span displacement and total internal energy of the RC columns are influenced by the following factors: spacing of the transverse bars (s_t), mass of the explosive charge at the entrance of the EDST (m_e), the load eccentricity (h_r), number of longitudinal bars (n_L), diameter of longitudinal bar (φ_L), strength of concrete (s_c), and diameter of the tie (φ_t). The spacing (s_t) and mass of the explosive charge (m_e) have the most important impact on the mid-span peak displacement and internal energy of RC columns.

In summary, the experimental and numerical analyses conducted in this study offer valuable insights into the impact of blast loading generated by the EDST on the dynamic behavior of circular RC columns. The laboratory experimental technique can be adopted for future experimental work.

Author Contributions: Conceptualization, D.L.; methodology, M.B.R., A.A. and B.B.; investigation, M.B.R., B.B. and A.A.; resources, D.L. and I.V.; data curation, M.B.R., B.B. and A.A.; writing—original draft preparation, M.B.R.; writing—review and editing, M.B.R. and B.B.; validation, M.B.R. and A.M.; supervision, D.L. and T.T. All authors have read and agreed to the published version of the manuscript.

Funding: This research received no external funding.

Data Availability Statement: The raw data supporting the conclusions of this article will be made available by the authors on request.

Acknowledgments: The authors are grateful to the staff of the Blast and Impact Protection Research Unit at the Royal Military Academy (RMA) in Brussels, as well as the Department of Structural Engineering and Building Materials in Ghent, for their support and assistance in performing the experimental work.

Conflicts of Interest: The authors declare no conflicts of interest.

References

1. Report on Improvised Explosive Device (IED) Incidents. Available online: <https://reliefweb.int/report/world/report-improvised-explosive-device-ied-incidents-january-june-2023> (accessed on 17 July 2023).
2. National Consortium for the Study of Terrorism and Responses to Terrorism START. Global Terrorism Database 2017. Available online: <https://www.start.umd.edu/gtd/> (accessed on 20 July 2023).
3. Tagel-Din, H.; Rahman, N.A. Simulation of the Alfred P. Murrah federal building collapse due to blast loads. In Proceedings of the AEI 2006: Building Integration Solutions—Proceedings of the 2006 Architectural Engineering National Conference, Omaha, Nebraska, 29 March–1 April 2006; Volume 2006, p. 32. [CrossRef]
4. United States of America. UFC 3-340-02 Structures to Resist the Effects of Accidental Explosions. Unified Facilities Criteria. No. September, 2008, pp. 1–12. Available online: https://www.wbdg.org/FFC/DOD/UFC/ufc_3_340_02_2008_c2.pdf (accessed on 20 January 2023).
5. U. S. Army. Fundamentals of Protective Design for Conventional Weapons. Technical Manual 1986, TM 5-855-1. Available online: <https://www.nrc.gov/docs/ML1019/ML101970069.pdf> (accessed on 21 January 2023).
6. Momeni, M.; Hadianfard, M.; Bedon, C.; Baghlani, A. Damage evaluation of H-section steel columns under impulsive blast loads via gene expression programming. *Eng. Struct.* **2020**, *219*, 110909. [CrossRef]
7. Swisdak, M.M. Simplified Kingery Airblast Calculations. In Proceedings of the Twenty-Sixth DoD Explosives, Safety Seminar, Miami, FL, USA, 16–18 August 1994; Volume 17. Available online: <https://apps.dtic.mil/sti/pdfs/ADA526744.pdf> (accessed on 1 February 2023).
8. Abedini, M.; Zhang, C.; Mehrmashhadi, J.; Akhlaghi, E. Comparison of ALE, LBE and pressure time history methods to evaluate extreme loading effects in RC column. In *Structures*; Elsevier: Amsterdam, The Netherlands, 2020; Volume 28, pp. 456–466. [CrossRef]
9. Liu, Y.; Yan, J.; Huang, F. Behavior of reinforced concrete beams and columns subjected to blast loading. *Def. Technol.* **2018**, *14*, 550–559. [CrossRef]
10. Mutalib, A.A.; Hao, H. Development of P-I diagrams for FRP strengthened RC columns. *Int. J. Impact Eng.* **2011**, *38*, 290–304. [CrossRef]
11. Louar, M.A.; Belkassam, B.; Ousji, H.; Spranghers, K.; Kakogiannis, D.; Pyl, L.; Vantomme, J. Explosive driven shock tube loading of aluminium plates: Experimental study. *Int. J. Impact Eng.* **2015**, *86*, 111–123. [CrossRef]
12. Hargather, M.J.; Settles, G.S. Laboratory-scale techniques for the measurement of a material response to an explosive blast. *Int. J. Impact Eng.* **2009**, *36*, 940–947. [CrossRef]
13. Jacinto, A.C.; Ambrosini, R.; Danesi, R.F. Experimental and computational analysis of plates under air blast loading. *Int. J. Impact Eng.* **2001**, *25*, 927–947. [CrossRef]
14. Svingala, F.; Biss, M.; Hargather, M.; Settles, G. Laboratory-scale blast testing of materials using air-shock loading. In Proceedings of the APS Division of Fluid Dynamics Meeting Abstracts, Minneapolis, MA, USA, 22–24 November 2009; Volume 62, p. EM-002.
15. Hu, Y.; Chen, L.; Fang, Q.; Xiang, H. Blast loading model of the RC column under close-in explosion induced by the double-end-initiation explosive cylinder. *Eng. Struct.* **2018**, *175*, 304–321. [CrossRef]
16. Sherkar, P.; Shin, J.; Whittaker, A.; Aref, A. Influence of Charge Shape and Point of Detonation on Blast-Resistant Design. *J. Struct. Eng.* **2016**, *142*, 04015109. [CrossRef]
17. *ASCE-59-11; Blast Protection of Buildings*. American Society of Civil Engineers (ASCE): Reston, VA, USA, 2011.
18. Woodson, S.C.; Baylot, J.T. Quarter-scale building/column experiments. In *Advanced Technology in Structural Engineering*; American Society of Civil Engineers: Reston, VA, USA, 2000; pp. 1–8.
19. Braimah, A.; Siba, F. Near-Field Explosion Effects on Reinforced Concrete Columns: An Experimental Investigation. *Can. J. Civ. Eng.* **2015**, *45*, 289–303. [CrossRef]
20. Pearson, R.J.; Wisniewski, H.; Szabados, P.; Wilson, A.W. *The Effects of Thermal/Blast Synergism on the Nuclear Vulnerability of a Generic Aircraft Structure*; Ballistic Research Laboratory: Aberdeen Proving Ground, MD, USA, 1984.
21. Bryson, A.E.; Gross, R.W.F. Diffraction of strong shocks by cones, cylinders, and spheres. *J. Fluid Mech.* **1961**, *10*, 1–16. [CrossRef]
22. Segars, R.A.; Carboni, M.G. *A Shock Tube for Downselecting Material Concepts for Blast Protection, Part I: Description of the Shock Tube and a Comparison of Flush Mounted and Recess Mounted Pressure Sensors*; U.S. Army Natick Soldier Systems Center: Natick, MA, USA, 2008; Technical Report No. 01760–5000.
23. Courtney, E.; Courtney, A.; Courtney, M. Shock tube design for high intensity blast waves for laboratory testing of armor and combat materiel. *Def. Technol.* **2014**, *10*, 245–250. [CrossRef]
24. Abe, A.; Takayama, K.; Itoh, K. Experimental and numerical study of shock wave propagation over cylinders and spheres. *Comput. Eng.* **2001**, *30*, 209–218.
25. Janardhanraj, S.; Karthick, S.; Farooq, A. A review of diaphragmless shock tubes for interdisciplinary applications. *Prog. Energy Combust. Sci.* **2022**, *93*, 101042. [CrossRef]
26. Gel'fand, B.E.; Voskoboinikov, I.; Khomik, S. Recording the Position of a Blast-Wave Front in Air. *Combust. Explos. Shock Waves* **2004**, *40*, 734–736. [CrossRef]
27. Enstock, L.K.; Smith, P.D. Measurement of impulse from the close-in explosion of doped charges using a pendulum. *Int. J. Impact Eng.* **2007**, *34*, 487–494. [CrossRef]

28. Shi, Y.; Hao, H.; Li, Z.X. Numerical derivation of pressure-impulse diagrams for prediction of RC column damage to blast loads. *Int. J. Impact Eng.* **2008**, *35*, 1213–1227. [[CrossRef](#)]
29. Shi, Y.; Hao, H.; Li, Z.-X. Numerical simulation of blast wave interaction with structure columns. *Shock Waves* **2007**, *17*, 113–133. [[CrossRef](#)]
30. Aoude, H.; Dagenais, F.; Burrell, R.; Saatcioglu, M. Behavior of ultra-high performance fiber reinforced concrete columns under blast loading. *Int. J. Impact Eng.* **2015**, *80*, 185–202. [[CrossRef](#)]
31. Chen, L.; Hu, Y.; Ren, H.; Xiang, H.; Zhai, C.; Fang, Q. Performances of the RC column under close-in explosion induced by the double-end-initiation explosive cylinder. *Int. J. Impact Eng.* **2019**, *132*, 103326. [[CrossRef](#)]
32. Fujikake, K.; Aemlaor, P. Damage of reinforced concrete columns under demolition blasting. *Eng. Struct.* **2013**, *55*, 116–125. [[CrossRef](#)]
33. Kwaffo, I.; Abdallah, M.H.; Braimah, A. Experimental assessment of the residual capacity of axially loaded blast-damaged square RC columns. In *Structures*; Elsevier: Amsterdam, The Netherlands, 2022; Volume 40, pp. 469–484. [[CrossRef](#)]
34. Kyei, C.; Braimah, A. Effects of transverse reinforcement spacing on the response of reinforced concrete columns subjected to blast loading. *Eng. Struct.* **2017**, *142*, 148–164. [[CrossRef](#)]
35. Wu, Y.; Xie, Q.; Mu, C. Sensitivity Analysis of Factors Influencing the Blast Resistance of Reinforced Concrete Columns Based on Grey Relation Degree. *Sustainability* **2023**, *15*, 12285. [[CrossRef](#)]
36. Thai, D.K.; Kim, S.E. Numerical investigation of the damage of RC members subjected to blast loading. *Eng. Fail. Anal.* **2018**, *92*, 350–367. [[CrossRef](#)]
37. Patil, M.N.; Khurd, V.G. Effects of different reinforcement schemes and column shapes on the response of reinforced concrete columns subjected to blast loading. *Int. Res. J. Eng. Technol.* **2018**, *5*, 571–581.
38. Rhouma, M.B.; Kailou, A.; Maazoun, A.; Belkasssem, B.; Tysmans, T.; Lecompte, D. Numerical investigation of the blast performance of reinforced concrete columns subjected to close-in explosion. In Proceedings of the 6th International Conference on Protective Structures, Auburn, AL, USA, 13–18 May 2023; p. 1712.
39. Astarlioglu, S.; Krauthammer, T.; Morency, D.; Tran, T.P. Behavior of reinforced concrete columns under combined effects of axial and blast-induced transverse loads. *Eng. Struct.* **2013**, *55*, 26–34. [[CrossRef](#)]
40. Bao, X.; Li, B. Residual strength of blast damaged reinforced concrete columns. *Int. J. Impact Eng.* **2010**, *37*, 295–308. [[CrossRef](#)]
41. Xiong, Z.; Wang, W.; Wu, Y. Sensitivity Analysis of Factors Influencing Blast-like Loading on Reinforced Concrete Slabs Based on Grey Correlation Degree. *Materials* **2023**, *16*, 5678. [[CrossRef](#)]
42. Kuo, Y.; Yang, T.; Huang, G.-W. The use of a grey-based Taguchi method for optimizing multi-response simulation problems. *Eng. Optim.* **2008**, *40*, 517–528. [[CrossRef](#)]
43. Woodson, S.C.; Baylot, J.T. Structural Collapse: Quarter-Scale Model Experiments. 1999, p. 176. Available online: <https://erdclibrary.ercd.dren.mil/jspui/bitstream/11681/11271/1/TR-SL-99-8.pdf> (accessed on 20 March 2023).
44. Baylot, J.T.; Bevins, T.L. Effect of responding and failing structural components on the airblast pressures and loads on and inside of the structure. *Comput. Struct.* **2007**, *85*, 891–910. [[CrossRef](#)]
45. Chen, W.; Hao, H.; Chen, S. Numerical analysis of prestressed reinforced concrete beam subjected to blast loading. *Mater. Des.* **2015**, *65*, 662–674. [[CrossRef](#)]
46. Abedini, M.; Mutalib, A.; Raman, S.; Baharom, S.; Nouri, J.S. Prediction of Residual Axial Load Carrying Capacity of Reinforced Concrete (RC) Columns Subjected to Extreme Dynamic Loads. *Am. J. Eng. Appl. Sci.* **2017**, *10*, 431–448. [[CrossRef](#)]
47. Xu, K.; Deng, Q.; Cai, L.; Ho, S.; Song, G. Damage detection of a concrete column subject to blast loads using embedded piezoceramic transducers. *Sensors* **2018**, *18*, 1377. [[CrossRef](#)]
48. Vapper, M.; Lasn, K. Blast protection of concrete columns with thin strips of GFRP overlay. *Structures* **2020**, *25*, 491–499. [[CrossRef](#)]
49. *EN ISO 6892-1; Metallic Materials-Tensile Testing-Part 1: Method of Test at Room Temperature*. International Organization for Standardization: Geneva, Switzerland, 2009.
50. *EN 12390-3; Testing Hardened Concrete. Compressive Strength of Test Specimens*. CEN: Brussels, Belgium, 2019.
51. Optical Lenses from Nikon. Available online: https://www.nikon.fr/fr_FR/product/lenses/mirrorless/nikkor-z-50mm-f1.2-s (accessed on 1 June 2023).
52. PCB Dynamic Pressure Sensors for High Frequency Measurements. Available online: https://www.pcb.com/contentstore/mktgcontent/linkeddocuments/pressure/tm-prs-113b-102b_lowres.pdf (accessed on 21 March 2023).
53. Atoui, O.; Kechagiadakis, G.; Moumen, A.; Maazoun, A.; Belkasssem, B.; Pyl, L.; Lecompte, D. An Explosive Driven Shock Tube-Based Laboratory Scale Test for Combined Blast and Fragment Impact Loading. *Appl. Sci.* **2022**, *12*, 6854. [[CrossRef](#)]
54. Dobratz, B.M. *LLNL Explosives Handbook: Properties of Chemical Explosives and Explosives and Explosive Simulants*; Lawrence Livermore National Lab.(LLNL): Livermore, CA, USA, 1981. [[CrossRef](#)]
55. Dua, A.; Braimah, A.; Kumar, M. Experimental and numerical investigation of rectangular reinforced concrete columns under contact explosion effects. *Eng. Struct.* **2020**, *205*, 109891. [[CrossRef](#)]
56. Maazoun, A.; Matthys, S.; Atoui, O.; Belkasssem, B.; Lecompte, D. Finite element modelling of RC slabs retrofitted with CFRP strips under blast loading. *Eng. Struct.* **2022**, *252*, 113597. [[CrossRef](#)]
57. Wu, Y.; Crawford, J.; Lan, S.; Magallanes, J.M. Validation Studies for Concrete Constitutive Models with Blast Test Data. In Proceedings of the 13 International LS-DYNA Users Conference, Dearborn, MA, USA, 8–10 June 2014; pp. 1–12.

58. Yan, J.; Liu, Y.; Xu, Z.; Li, Z.; Huang, F. Experimental and numerical analysis of CFRP strengthened RC columns subjected to close-in blast loading. *Int. J. Impact Eng.* **2020**, *146*, 103720. [[CrossRef](#)]
59. Crawford, J.E.; Malvar, L.; Wesevich, J.; Valancius, J.; Reynolds, A.D. Retrofit of reinforced concrete structures to resist blast effects. *ACI Struct. J.* **1997**, *94*, 371–377. [[CrossRef](#)]
60. Javier, M.L.; Allen, R.C. Review of Strain Rate Effects for Concrete in Tension. *ACI Mater. J.* **2017**, *153*, 846–856. [[CrossRef](#)]
61. Malvar, L.J.; Crawford, J.E. Dynamic Increase Factors for Steel Reinforcing Bars. In Proceedings of the Twenty-Eighth DoD Explosives Safety Seminar, Orlando, FL, USA, 18–20 August 1998; pp. 1–18.
62. Gholipour, G.; Zhang, C.; Mousavi, A.A. Numerical analysis of axially loaded RC columns subjected to the combination of impact and blast loads. *Eng. Struct.* **2020**, *219*, 110924. [[CrossRef](#)]
63. Thilakarathna, H.M.I.; Thambiratnam, D.; Dhanasekar, M.; Perera, N. Numerical simulation of axially loaded concrete columns under transverse impact and vulnerability assessment. *Int. J. Impact Eng.* **2010**, *37*, 1100–1112. [[CrossRef](#)]
64. McCormick, J.; Nagae, T.; Ikenaga, M.; Zhang, P.; Katsuo, M.; Nakashima, M. Investigation of the sliding behavior between steel and mortar for seismic applications in structures. *Earthq. Eng. Struct. Dyn.* **2009**, *38*, 1401–1419. [[CrossRef](#)]
65. Kostopoulos, V.; Kalimeris, G.; Giannaros, E. Blast protection of steel reinforced concrete structures using composite foam-core sacrificial cladding. *Compos. Sci. Technol.* **2022**, *230*, 109330. [[CrossRef](#)]
66. Schwer, L.; Teng, H.; Souli, M. LS-DYNA air blast techniques: Comparisons with experiments for close-in charges. In Proceedings of the 10th European LS-DYNA Conference, Würzburg, Germany, 15–17 June 2015; pp. 15–17.
67. Narong, O.L.C.; Sia, C.K.; Yee, S.K.; Ong, P.; Zainudin, A.; Nor, N.H.M.; Hassan, M.F. Optimisation of EMI shielding effectiveness: Mechanical and physical performance of mortar containing POFA for plaster work using Taguchi Grey method. *Constr. Build. Mater.* **2018**, *176*, 509–518. [[CrossRef](#)]

Disclaimer/Publisher’s Note: The statements, opinions and data contained in all publications are solely those of the individual author(s) and contributor(s) and not of MDPI and/or the editor(s). MDPI and/or the editor(s) disclaim responsibility for any injury to people or property resulting from any ideas, methods, instructions or products referred to in the content.